17th August 2020

Evolution of normal fault displacement and length as the continental lithosphere stretches

Sophie Pan[1*], Rebecca E. Bell[1], Christopher A-L. Jackson[1], John Naliboff[2]

[1]Basins Research Group (BRG), Earth Science and Engineering, Imperial College, Prince Consort Road, London, SW7 2BP

[2]Department of Earth and Environmental Science, New Mexico Institute of Mining and Technology, NM, USA

[*]Corresponding author: Sophie Pan (sophie.pan16@imperial.ac.uk)

HIGHLIGHTS

- 7.2 Myrs after rift initiation, fault trace lengths were established to their near-full lengths
- At 28.5 Myrs, fault *segment* throw profiles were symmetric, but overall fault *system*s were asymmetric
- In the last 67% of rifting, antithetic faults located in stress shadows remained inactive and under-displaced
- We suggest faults grow in alternating phases of fault lengthening and displacement accumulation
- Our model suggests the frequently observed D-L scatter reflects fault growth and maturity

ABSTRACT

Continental rifting is accommodated by the development of normal fault arrays. Fault growth patterns control their related seismic hazards, as well as influencing the tectonostratigraphic evolution, resource extraction and CO_2 storage potential of rifts. Our understanding of fault evolution is largely derived by observing the final geometry and displacement (D)-length (L) characteristics of active and inactive fault systems, and by making subsequent inferences on their kinematics. We rarely consider how these properties change through time, and how the growth of individual fault *systems* relates to the temporal evolution of their host *arrays*. Here we use 3D seismic reflection and borehole data from the Exmouth Plateau, NW Shelf, Australia to determine the growth of rift-related, crustal-scale fault systems and arrays over geological timescales ($>10^6$ Ma). The excellent-quality seismic data allows us to reconstruct the entire Jurassic-to-Early Cretaceous fault array over a large area (~1200 km^2). We find that fault trace lengths were established early, within the first ~7.2 Myr (8%) of rifting, and that along-strike migration of throw maxima towards the centre of individual fault systems occurred after ~28.5 Myr (33%) of rifting. We propose that D and L may scale linearly, but increase via alternating phases of fault lengthening and displacement accumulation. Growth trajectories produce inflections in D-L space, reflecting times when fault lengths and/or displacement saturate a given rock volume, possibly controlled by crustal thickness. At the array-scale, faults located in stress shadows become inactive and appear under-displaced relative to adjacent larger faults, onto which strain localises as rifting proceeds. This implies that the scatter frequently observed in D-L plots can simply reflect fault growth and array maturity. We show that by studying complete rift-related normal arrays rather than individual faults, we can better understand how faults grow and more generally how continental lithosphere deforms as it stretches.

1. INTRODUCTION

The formation of extensional basins is controlled by the development of normal faults. Large, basin-bounding fault *systems* typically grow by the initiation, propagation, interaction, and linkage of smaller fault *segments* (e.g. Peacock and Sanderson, 1991; Anders and Schlische, 1994; Trudgill and Cartwright, 1994; Dawers and Anders, 1995; McLeod et al., 2000). A kinematically linked network of fault segments and systems comprise a fault *array*. Fault arrays evolve in response to co- and interseismic stress feedbacks between the constituent segments and systems; this can lead to the temporal progression from numerous, short, low-displacement segments to a few, long, high-displacement systems ('strain localisation'; Cowie, 1998; Gawthorpe and Leeder, 2000) (Figure 1).

As strain localisation is often associated with an increase in basin subsidence rate, the temporal and spatial evolution of fault arrays are reflected in changes in rift physiography, and the location and rate of generation of accommodation (e.g. Dawers and Underhill, 2000, McLeod et al., 2000). The way in which fault arrays grow therefore strongly influences the size, shape, and distribution of sedimentary depocenters and drainage catchments, which in turn control the location of various energy resources, groundwater reservoirs, and potential CO_2 storage sites (e.g. Gawthorpe and Leeder, 2000).

Mechanical interactions between adjacent faults profoundly affects the stress-dependent nature of earthquakes in potentially hazardous, seismically active regions (e.g. Harris, 1998; Stein, 1999; Allmendinger et al., 2000; Dolan et al., 2007; Nicol et al., 2010; Mildon et al., 2019). An improved understanding of both long-term fault displacement patterns from ancient fault arrays imaged in seismic reflection data, together with short-term earthquake slip rates most commonly derived from regions of active extension, would allow us to characterise fault growth and interactions over multiple timescales, from a few seconds up to tens-to-hundreds of millions of years (Allmendinger et al., 2000; Nicol et al., 2010; Nicol et al., 2006; Scholz and Gupta, 2010; Nicol et al., 2019). However, our current understanding of fault growth largely stems from detailed studies of individual fault *systems* (e.g. Walsh et al., 2002; Nicol et al., 2005; Jackson and Rotevatn, 2013; Fossen and Rotevatn, 2016; Nicol et al., 2016; Childs et al., 2017; Jackson et al., 2017), rather than rift-scale fault *arrays*, thereby often overlooking the important role fault interactions and stress feedbacks may play in controlling the early stages of fault and rift development.

Historically, fault growth models have been proposed based on field and subsurface observations of the final geometry of ancient faults, often in the absence of kinematic constraints on how the faults evolved. The key geometric relationship that has been used is the relationship between fault length (L) and maximum fault displacement (D):

$$D_{max} = cL^n$$

Where *c* represents the scaling D/L ratio and *n* represents an exponent value argued to vary from 2 (Watterson, 1986; Walsh and Watterson, 1988) to 1 (Cowie and Scholz, 1992; Dawers et al., 1993; Schlische et al., 1996), with a value of 1 indicating a linear scaling law (i.e. self-similarity) (Fig 2) (see also Marrett and Allmendinger, 1991). The exponent *n* remains unresolved due to the significant amount of scatter in global D-L profiles (Fig. 2) (Cowie and Scholz, 1992; Dawers et al., 1993; Scholz et al., 1993, Cartwright et al., 1995; Nicol et al., 1996; Cladouhos and Marrett, 1996; Schlische et al., 1996), which may reflect the natural geological variations between study areas (e.g. host rock mechanical properties), and uncertainties in data quality and sampling approaches (Gillespie et al., 1992; Walsh and Watterson, 1988; Kim & Sanderson, 2005; Walsh et al., 2017). However, it is possible that variations in *n* reflect fundamentally differing styles of fault growth. For example, current conceptual models suggest that faults may grow by either the: (i) 'propagating model', in which fault displacement and length simultaneously increase, producing a linear growth trajectory (Fig 2; e.g. Walsh and Watterson, 1988; Cartwright, 1995; Walsh et al., 2003); or (ii) the 'constant length model', in which faults reach their near-full lengths rapidly before significant displacement accumulation, producing an initially shallow gradient trajectory on D-L plots as the fault lengthens, followed by a near vertical trajectory as the fault accumulates displacement (Fig 2; e.g. Walsh et al., 2002; Meyer et al., 2002; Nicol et al., 2005; Nicol et al., 2016; Childs et al., 2017; Jackson et al., 2017; Rotevatn et al., 2019). The two fault models may represent end-members (Fossen 2016; Childs et al., 2017), leading to the proposition of a hybrid growth model (Rotevatn et al., 2019), in which faults initially lengthen via propagation and linkage for 20-30% of the fault's lifespan, before later accumulating displacement for the final 70-80%. However, the implications of the constant/hybrid model in D-L space are not yet clear.

Our current understanding of fault segment, system and array growth is largely geometric and based on observations from modern extensional basins or ancient basins imaged in seismic reflection data. There are very few studies that provide a *temporal* framework for the growth of normal fault segments and systems (e.g. Tvedt et al., 2016; Meyer et al., 2002). This is mainly due to the lack of age-constrained growth strata to record the timing of fault activity (e.g. Dawers et al., 1993; Schlische et al., 1996; Peacock and Sanderson, 1991). There are even fewer attempts to determine the evolution of entire fault arrays at the rift scale (e.g. Claringbould et al., 2017). We suspect this may reflect the time-consuming effort required to manually interpret many seismically imaged normal faults, and to subsequently extract their related geometric properties (i.e. displacement, length). As a result, most studies focus on the growth of large, basin-bounding structures (i.e. major fault systems; e.g. McLeod et al., 2000), whilst ignoring smaller, intra-basin ones (i.e. fault segments; e.g. Tvedt et al., 2002).

Here we use 3D seismic reflection and borehole data from the Exmouth Plateau, NW Shelf, Australia to determine the growth of rift-related, crustal-scale fault systems and arrays over geological timescales ($>10^6$ Ma). This study area was subject to Late Triassic-to-Early Cretaceous extension, forming extremely well-defined and well-imaged normal faults, half-grabens, and grabens (Exon and Willcox., 1978; Mutter and Larson, 1989). The large extent of the study area (1200 km^2) is of a comparable size to areas of active continental extension containing large, seismogenic fault arrays, including East Africa (Baker et al., 1972; Albaric et al., 2010; Poggi et al., 2017), Central Italy (Luccio et al., 2010; Collettini and Barchi, 2002; Roberts and Michetti, 2004; Cowie et al., 2013), Central Greece (King et al., 1985; Bell et al., 2009; Taylor et al., 2011), SE Russia (Logatchev and Zorin, 1992; Mats, 1993), western Turkey (Seyitoglu, 1996), and the western USA (Hamilton, 1987; Thatcher et al., 1999). This makes our study area an excellent ancient analogue with which to better understand the geological evolution of areas of active continental extension.

To the best of our knowledge, this study is the first to quantify the temporal evolution of a complete rift-scale fault array using geometric observations of all seismically resolvable faults. We first define the present-day structure of the fault array (i.e. the final product of rifting). Second, we use depocentre mapping (via the use of time-thickness maps known as isochrons) and fault displacement backstripping to reconstruct the geometry of the entire fault array at an earlier stage of rifting. This allows us to determine the growth trajectory of individual fault segments and systems, which we then compare to global D-L datasets (Figure 2). Based on our results, we propose a model for the growth of fault arrays. Our model links our current knowledge of the styles of segment- and system-scale growth (i.e. propagating vs constant length models) to the development of the larger fault array. Our model provides an explanation for the long-recognised scatter observed in global D-L datasets and sheds light on how continental lithosphere stretches during early rifting (e.g. Cowie and Schultz, 1992; Cartwright et al., 1995; Kim and Sanderson, 2005; Rotevatn et al., 2019).

2. GEOLOGICAL HISTORY

The Thebe dataset is located on the Exmouth Plateau (Exon and Willcox 1978) portion of the Northern Carnarvon Basin, NW Shelf of Australia (Geoscience Australia 2014) (Fig. 3a). Formation of the Northern Carnarvon Basin initiated during the Carboniferous to Permian in response to the breakup of Pangea, with episodic rifting continuing until the Late Cretaceous (Stagg and Colwell, 1994; Driscoll and Karner, 1998). Late Triassic rifting produced NE-trending sub-basins (Fig 3a), until a phase of regional uplift in the Callovian (Barber 1988; Pryer et al., 2002; McCormack and McClay, 2013; Metcalfe, 2013). Extension renewed in the Late Jurassic as the Argo block separated from Gondwana, culminating with seafloor spreading and the opening of the Argo Abyssal Plain during the Hauterivian (Tindale, 1998; Heine and Muller, 2005; Gibbons et al., 2012; Metcalfe, 2013). The period of Late Jurassic-to-Early Cretaceous rifting was also characterised by the formation of NE-SW-striking faults, locally reactivating Late Triassic faults (e.g. Jitmahantakul and McClay, 2013; Magee et al., 2016).

The stratigraphic framework of the Exmouth Plateau consists of a thick, Upper Triassic pre-rift succession of the fluvio-deltaic and marginal marine deposits of the Mungaroo Formation

(Fig 4) (Tindale et al., 1998; Driscoll and Karner, 1988; Longley et al., 2002). From the Late Triassic to Late Jurassic, a syn-rift succession comprised of shallow marine claystone and limestone of the Brigadier Formation (Late Triassic) and marine claystones of the Athol and Murat formations (Early to Middle Jurassic), were deposited within fault-bound, rift-related depocentres (e.g. Stagg and Colwell, 1994; Tindale et al., 1998; Stagg et al., 2004; Longley et al., 2002). During the Late Jurassic to Early Cretaceous, uplift resulted in a decrease in water depth and an influx of interbedded shale and fluvial deltaic sands of the Barrow Group (Fig 4) (Boyd et al., 1992). In association with the subsequent subsidence, a major transgression resulted in the deposition of a thick succession of post-rift marine deposits of the Muderong Shale, Windalia Radiolarite and Gearle Siltstone, which are collectively known as the Winning Group (Hocking, 1987; Driscoll and Karner, 1998) (Fig. 4).

3. DATASET AND METHODOLOGY

3.1. Seismic reflection and well data

Our database comprises a pre-stack time-migrated 3D seismic reflection survey (HEX07B) located in the WA-346-P permit area, and two wells (Thebe-1 and Thebe-2) (Fig. 3). The seismic data images to depths of ~4.5 s TWT (~3.7 km) and covers 45 km x 39 km, providing a total areal extent of 1200 km^2. Crosslines are spaced at 25 m and inlines at 12.5 m. The dominant frequency is 45 Hz at the depth of the studied fault array at Thebe-1. From time-depth plots derived from well checkshot data, we estimate the average velocity to be 2480 m/s within the Jurassic syn-rift units; when combined with frequency data, this results in an estimated spatial vertical resolution of c. 14 m ($\lambda/4$). Overall, the data quality is excellent throughout and enables a high-resolution analysis of fault structure and evolution.

The Thebe-1 and Thebe-2 wells are drilled in the footwalls of tilted fault blocks (Fig 3b) and collected a standard well-log suite (e.g. gamma ray, density, sonic, checkshot and biostratigraphic data). We choose to present our measurements of fault throw in time (ms TWT) rather than depth, given we are primarily interested in the relative changes of throw rather than absolute values (cf. Tvedt et al., 2016; Jackson et al., 2017), and we do not have a high-resolution 3D velocity model to constrain along-strike changes in velocity. To estimate depth in metres from observations in ms TWT, we have used checkshot data from wells that define a polynomial relationship between time and depth. We have not attempted to decompact our throw values as the loss of throw is likely relatively low (< 15%) in mixed sand-shale growth sequences that characterise much of the syn- to post-rift succession of the Exmouth Plateau (cf. Taylor et al. 2008); we also lack information on sediment compaction parameters from the two wells. For better comparison with global D-L compilations, we converted our throw data to displacement data by assuming an average fault dip of 60°, as this is an average for the faults in this area.

3.2. Structural framework

We mapped ten horizons throughout the seismic reflection volume (labelled H1 – H10; see ages in Fig 4) to delineate the present basin structure and then unravel the fault evolution. Fault interpretation was conducted throughout the seismic volume, aided by overlaying the dip attribute onto mapped horizons (i.e. the deviation of a seismic reflection from a horizontal plane) (Chopra and Marfurt, 2007). We measured the tip-to-tip lengths of all seismically resolvable, individual fault segments at the base of the syn-rift, given this structural level captured most of the rift-related strain (see Fig 1 for definitions). In D-L plots, we show the scaling properties of individual segments, as well as fault systems (F1-F3). We classify faults systems as *major* (F1-

F3) if their throw is >150 ms (TWT) and *minor* if their throw is <150 ms TWT (labelled on Fig 3b).

Fault throw was constrained by measuring the vertical distance between horizon cut-offs in the footwall and hanging wall on seismic profiles trending perpendicular to local fault strike (cf. McLeod et al., 2000; Tvedt et al., 2013). Values are taken every 100 - 400 m along the fault depending on the structural complexity and throw variability along the fault. In the presence of erosional footwall fault scarp degradation and fault-related ductile (continuous) deformation, the horizon cut-offs are projected towards the fault plane along the regional structural trend (e.g. Long and Imber, 2010; Whipp et al., 2014, Bell et al., 2014; Wilson et al., 2015; Barrett et al. submitted).

3.3. Constraining rift evolution

To constrain the fault array evolution, we use isochron (time-thickness) mapping and throw backstripping techniques, which are kinematically constrained by our mapped age-constrained horizons (H2, H3, H4, H8, H9 and H10; Fig 4). The ages of three syn-rift horizons are not constrained by the wells (H5, H6 and H7); their ages are therefore inferred based on an assumption of constant sedimentation rates between bounding, age-constrained horizons (Fig 4). We define H2 (Top Mungaroo; 208.5 Ma) as the base syn-rift (i.e. the start of rifting), consistent with other publications (e.g. Stagg et al., 2004; Tindale et al., 1998), given we observe no across-fault sediment thickness changes between H1 and H2 (Figure 5). Fault activity ceases at H9 (Top Muderong; 113 Ma), based on observations of no across-fault changes in thickness above H9, which we thus define as top syn-rift (i.e. the end of rifting). Our ages for top and base syn-rift give a total rift duration of ~85.5 Myr (Fig 4). We produced six isochron maps within the syn-rift interval (SU1–6; Figs 4 and 6), which we use to constrain patterns of fault-controlled subsidence and thus fault growth (Thorsen, 1963; McLeod et al., 2000; Jackson and Rotevatn, 2013).

We use fault throw backstripping to constrain the style and patterns of fault growth (Childs et al., 1993; Rowan et al., 1998; Dutton and Trudgill, 2009, Jackson et al., 2017). Throw backstripping involves the subtraction of fault throw at multiple stratigraphic levels to determine the throw accumulated during deposition of the backstripped unit (see Chapman and Meneilly, 1991). Faults can be backstripped using the 'original method' or the 'modified method'. The 'original method' directly subtracts throw across a shallower horizon from that of the deeper horizon (Chapman and Meneilly, 1991; Petersen et al., 1992), making no assumptions about fault growth style. The 'modified method' subtracts the maximum throw along the horizon from the entire fault surface. This method implicitly assumes that the studied fault grew in accordance with the propagating fault model (Rowan et al., 1998; Jackson et al., 2017). In this study we use the original method to avoid any *a priori* assumption of the style of fault growth. We then compare our throw backstripping results with depocenter lengths revealed by isochrons; this allows us to assess fault length at different points in the rift history (cf. Jackson and Rotevatn, 2013; Jackson et al., 2017).

The Exmouth Plateau was sediment-starved (i.e. underfilled) during Jurassic extension (Marshall and Long, 2013; Gartrell et al., 2016). Because of this, accommodation associated with the very earliest stage of extension may have been unfilled, meaning: (i) we cannot determine if any observed fault lengthening occurred by segment linkage or tip propagation (infilling sediments do not exist to record this); and (ii) our measured trace-lengths may thus have been established earlier (i.e. more quickly) than estimated, such that our estimates should be seen as maximum possible values (Jackson et al., 2017; Lathrop et al. submitted).

4. RESULTS

4.1. Structural framework

4.1.1. Time-structure maps

We first describe the present-day structure of the study area (Fig 6 and Fig 7). We mapped 150 faults over an area of 45 x 39 km that displace the 208.5 Myr base syn-rift horizon (H2, Top Mungaroo); this surface records the total cumulative rift-related strain of the fault array. The base syn-rift surface also contains the largest number of faults. Faults are strongly segmented, being either hard- and soft-linked across relays (Fig 6a). Fault trace lengths at the structural level of H2 (Top Mungaroo) range from c. 300 m to >15000 m, with the largest faults extending beyond the study area (Fig 6).

A fault map and rose diagram (Fig 7) reveal the strike and dip direction of the syn-rift fault array at the structural level of H2. Major NE-SW-striking faults define the fault array, with a minor set of E- dipping, N-S striking faults (Fig 7). The main NE-SW-striking population comprises 86 E- dipping faults and 57 W- dipping faults, although major faults (i.e. F1-F3) exclusively dip westwards, whereas the remaining antithetic faults dip eastward (Figure 7). The antithetic E- dipping faults are spaced ~2 km, whereas fault spacing for the major, W- dipping fault systems is 12-16 km (labelled on Fig 3b).

Time-structure maps reveal a reduction in faulting in the shallower structural levels as faults die-out upwards, with only the major fault systems (F1-F3) present at the top syn-rift horizon (H9; Top Muderong) (Fig 5, Fig 6f). These major fault systems extend upward above H10, where they link to normal faults contained in a widespread polygonal fault array (Fig 5). A series of small en-echelon faults occur at the structural level of H6 (~143 Myr) and H7 (~141 Myr), whereas at deeper levels there is a continuous N-S-striking fault. This observation suggests that faults splay vertically upwards as well as horizontally (i.e. at lateral fault tips) (Fig 6c and d). Cross-cutting relationships suggest that the N-S-striking faults formed before the NE-SW-striking fault population (Fig 5, Fig 6a).

4.1.2. Throw distribution

Maximum throw on the syn-rift fault array varies from 10 to 650 ms TWT (10 – 670 m) (Figure 8a). Throw varies along-strike on major fault systems F1-F3, with maximum throw (up to 650 ms TWT) typically occurring near their centres. Throw gently decreases to zero at the tips of fault systems (e.g. F2-a, Fig 8a). Individual segments forming the fault systems may show relatively steep throw gradients towards their tips (e.g. F2-b; see Fig 1 for definitions). Strain is distributed on several splay faults at the ends of fault systems (Figure 9a for location). Overall, the aggregate throw of major faults produce a broadly coherent, symmetric throw shaped profile with a gradual decrease in throw towards the tips (Figure 8a).

In detail, however, throw minima exist along many major fault systems (e.g. F2-a, F2-b, F3-b), with these minima tending to correlate with areas where fault systems change strike (F2, F3; Fig 8a). The relay zone between F3-a and F3-b shows a decrease in throw when fault segments overlap (Fig 8a). These two observations suggest major fault systems were previously segmented, at least at this structural level (Figure 8a).

In contrast to the major fault systems, minor fault systems typically have a uniform throw value along strike (ranging from 20-80 ms TWT) but exhibit an abrupt decrease in throw towards their tips (Figure 8a). Local throw minima on minor faults also correspond to abrupt changes in the strike, again suggesting a history of fault linkage via segment linkage (Figure 6a).

4.2. Rift evolution

In order to determine the growth of the fault array, we now quantify the activity of individual fault systems through the use of isochron maps and throw backstripping.

4.2.1. Isochron analysis

Within the earliest resolvable time period, SU1 (from 208.5 to 201.3 Ma; i.e. capturing fault activity during the first 7.2 Myrs of rifting), we observe across-fault thickening (~100 ms TWT) on all major faults (F1-F3; Fig 9a). These fault-controlled depocenters span the entire present-day fault trace length, indicating that major faults had already reached their near-final length during the first 7.2 Myr of the ~85.5 Myr rift history (i.e. only 8% of the total rift duration). Thick (up to 200 ms TWT or 225 m), mound-shaped features are present in the hanging walls of F1, F3-a and F3-b, which we interpret as the deposition of fault scarp-derived talus (Fig 9a) (Bilal et al., 2019; Barrett et al., 2020). Fault scarp-derived deposits provide further evidence that the faults were active during this period. These deposits also suggest that fault slip rates outpaced sediment accumulation rates, and that at-surface relief formed which was then eroded.

Thickness variations in SU2 (Figure 9b) show that fault-controlled depocenters persisted adjacent to the major fault systems F1-F3 (from 201.3 to 163.5 Mya; i.e. capturing fault activity during the subsequent 37.5 Myrs of rifting). SU2 depocenters are wider (normal to fault strike) than those in SU1, and show a greater thickness increase up to 3.5 km away from the fault, indicating increased hanging wall flexure (Fig 9b). SU2 is thickest in the middle of the depocenters adjacent to F3-a and F3-b (<170 ms TWT) instead of immediately adjacent to the bounding faults, which we attribute to the underlying scarp-derived sedimentation in SU1 leading to an apparent reduction in the thickness of deposits in SU2 (Fig 9b, Fig 5). Although there is an overall thickness increase across both F3-a and F3-b (~120 ms TWT), high thickness variations (up to ~220 ms TWT) are distinct across F3-a and F3-b, separately indicating that the fault segments were soft-linked and separated by a relay zone (Fig 9b). Thickness variations also suggest that F2-a and F2-c segments were active during the SU2 time interval, but a lack of thickness changes in association with F2-b suggest that the F2 system was not hard-linked at this time (Figure 9b).

Within SU3 (from 180 to 143 Mya; i.e. capturing fault activity during the subsequent 37 Myrs of rifting) we observe a thickness increase of 100 ms TWT across *all* segments of F2. This is in contrast to activity within SU2, where no thickness changes occurred across the faults central segment (F2-b), indicating that by 37 Myrs after the onset of rifting, F2 had hard-linked to form a through-going system (Fig 9c). Additionally, thickening across both F3-a and F3-b segments suggest that F3 was now acting as a single, hard-linked fault system that was principally growing via the accumulation of displacement at the expense of lengthening (Figure 9c). In summary, F2 and F3 had grown to the maximum lengths after only 33% of the total rift duration, achieving this by segment linkage and relay breaching. This style of growth resulted in the development of abandoned splays in their hanging wall.

SU4 (from 143 to 141 Mya; i.e. capturing fault activity during the subsequent 2 Myrs of rifting) shows a significant thickness increase across F2, indicating this major structure was active at this time. SU5 (from 141 to 138 Mya; i.e. capturing fault activity during the subsequent 3 Myrs of rifting) shows no thickness variations across F1 and F2, suggesting that these structures were inactive by this time (Fig 9e). F3-a also became inactive as evidenced by constant across-fault thickness of SU5. In contrast, the southern part of the fault system remained active (F3-c and F3-d), defining a relatively wide (~4 km across strike) depocenter. SU6 (from 138 to 123 Mya; i.e. capturing fault activity during the subsequent 15 Myrs of rifting) shows that nearly all the northern faults were inactive during this time, as only the southern segments of F2 and F3 are associated with thickness variations. However, as these variations appear broad and regional, occurring on a length-scale larger than individual faults (Figure 9f), and given that the timing of deposition of SU6 coincides with a period of widespread regional subsidence along the margin (Hocking, 1987; Driscoll and Karner, 1998), we infer that F3-c, F3-d, F2-b, F2-c may be less active than the spatially related thickness changes suggest.

4.2.2. Fault throw backstripping

Isochrons qualitatively reveal that fault lengths were established relatively quickly, as fault-controlled depocenters nearly span across their entire present-day fault trace lengths within the earliest resolvable slip increments (Fig 9a, 9b). This style of growth is consistent with the constant-length model of fault growth, hence the original rather than modified method is considered more appropriate to backstrip the fault array (e.g. Jackson et al. 2017; see methodology section). H3 is not present across the entire fault array due to footwall erosion (see Figure 7a), therefore backstripping is undertaken to the next resolvable increment H4 (180 Ma) to view an intermediate stage of array evolution (i.e. at 33% of the total rift duration). As a result, we can gain a view of rift-related strain after 33% (Fig 8b) and 100% of the rift duration (Fig 8a). Our results show that by 33% of rift history, major faults F1, F2, and F3 had accumulated maximum throws of throws of 261, 181 and 365 ms TWT (c. 261, 183, 372 m) respectively (Fig 8b); this is approximately half of the present-day throw.

Throw accumulation was relatively uniform (averaging ~200 ms TWT) along F1, with a relatively abrupt decrease in throw occurring near a throw minima located at 16.3 km along the fault (Fig 8b). This minima corresponds to a small hanging wall splay and a subtle change in fault strike, thus we infer it defines a relay that was breached before this backstripped interval (i.e. before 33% of the rift duration; Fig 8b, Fig 3b). F1 continues north beyond the seismic dataset, so we cannot tell whether the maximum throw on this structure is located further north; however, extrapolation of the throw gradient at the northern end of F1 suggests this is not the case (Figure 8b). Our results indicate that during the latter part of rifting (33-100% of the rift duration), F1 accumulated throw near its centre without appreciable lengthening. Our present-day throw-length plot shows a broadly symmetric, bell-shaped profile, with no strong indication of paleo-segmentation (i.e. displacement minima; Fig 8a).

During the initial stage of rifting, F2 exhibited a similar throw distribution as F1, in that throw (average of 130 ms TWT) was fairly evenly distributed along its constituent segments (F2-a, F2-b and F2-d; Fig 8b). The throw minima between F2-a and F2-b suggests that these segments were not geometrically linked at this time. Instead, F2-b develops alongside two small hangingwall splays (pink and brown in Fig 8b). At this time, a small splay (purple in Fig. 8b; see Figure 3 for corresponding map) appears to be kinematically interacting with fault segments F2-c and F2-d, given they together define a throw profile that shows a gradual southward increase in throw (Figure 8b). However, the purple splay and F2-d appear to have been abandoned during the latter phase of rifting (33-100% of rift duration); instead, F2-c gained significant throw (from ~80 to 330 ms TWT) and hard-linked with F2 as rifting continues (Figure 8). During the latter phase of rifting, F2-b also accumulated a significant amount of displacement (up to 550 ms

TWT) to produce the relatively symmetric, bell-shaped throw profile that presently characterises F2 (Fig 8a).

Backstripping of F3 reveals that during the initial stage of rifting, a series of throw maxima were located towards the northern portions of segments F3-a, F3-b and F3-c. Whereas F3 still displays a generally symmetric throw profile, its constituent segments are defined by a rather irregular, asymmetric throw profile (Fig 8b). Throw minima (e.g. between F3-a and F3-b) indicate relay zones that was breached prior to this time-step (Fig 8b). By comparing the throw distribution after c. 33% of the rift history with that presently observed (Figure 8a), our results show that during the last 67% of rift history, the asymmetric and irregular profile of fault system F3 evolved to have a symmetric, bell-shaped profile, with the throw maxima migrating towards the present centre of the fault.

Backstripping of minor faults show that fault lengths and throw distribution remained relatively similar during the latter 67% of the rift history (Fig 8). A number of minor faults appeared to have died-out before the deposition of H4 (180 Ma; Top Murat Siltstone); however, ductile or so-called *continuous* deformation, make offset difficult to determine at H4. Our interpretation that the minor faults became inactive <28.5 Myr into the rift event is supported by isochron data, which shows that post-SU2 units do not thicken across them, as well as seismic cross-section evidence that show minor fault tipping-out below H4.

5. DISCUSSION

Timescales of fault growth

Our results clearly demonstrate that many of the fault’s established their near-final length relatively early in the ca. 85.5 Myr rift history. Throw backstripping quantitatively shows that for many of the faults, their lengths were essentially fixed after only ca. 33% of the total rift duration (Fig 8); isochron analysis suggest that fault length establishment may have occurred after as little as 8% of the total rift duration (Fig 9a). This duration is similar to that documented by Walsh et al., (2002), Jackson et al., (2017), and Rotevatn et al., (2019), who show that faults typically establish their near-final lengths within c. 30% of their total growth history. Our results show that this early stage of fault lengthening could be even shorter (i.e. 8%). Whereas current models of fault growth typically focus on the development of the largest fault *systems* within a given region, we note that some of the minor, antithetic faults located *between* the larger fault systems, are relatively long (i.e. >20 km) with low displacements (<30 m). Although we cannot directly establish if these structures were lengthening and/or accumulating displacement immediately prior to their death, observations of their long trace lengths, paleo-segmentation on time-structure maps (Fig 6), thickness variations from isochrons (Fig 9) and throw minima from throw backstripping (Fig 8), suggest that prior to becoming inactive, the majority of growth was occupied by fault lengthening via segment linkage. We suspect that these long, low-displacement faults may be 'fossilised' in their early stages, providing a snapshot of fault development before localisation and displacement accrual – we discuss this later in the context of our updated model.

The last c. 67% (and possibly up to c. 92%) of the 85.5 Myr rift history was characterised by strain localisation and displacement accumulation on the major fault systems (F1-F3). Strain localisation onto larger faults that are ultimately active for longer than smaller faults is also seen in the Inner Moray Firth, North Sea (Nicol et al., 1997; Walsh et al., 2003), and the Timor Sea, NW Shelf of Australia (Meyer et al., 2002), and in numerical (e.g. Cowie et al., 1995; Cowie, 1998; Gupta et al., 1998; Naliboff et al., 2020) and physical models (e.g. Ackermann et al., 2002; Mansfield and Cartwright, 2001). Our results demonstrate that the pattern of displacement accumulation and/or localisation itself is not straightforward, due to complex fault interactions that result in relay breaching and associated splay abandonment (e.g. Fig 9). Isochrons and throw backstripping reveal a distributed fault array that is initially composed of fault systems with multiple displacement maxima and minima. Detailed backstripping analyses show that in the early stages of fault development, fault segments exhibited profiles that were broadly symmetric (i.e. throw was greatest at the fault centres and decreases towards their tips). At the end of rifting (captured by present day geometry), throw profiles of fault systems are also symmetric. However, at an intermediate stage of rifting (33% of total rift duration; Figure 8b), while fault *segments* are symmetric, the overall fault *system* in which they are contained exhibited an irregular, asymmetric throw profile. At this stage of rifting, we observe multiple examples of splay abandonment (e.g. F2-c) related to strain localisation onto more optimally positioned fault segments that lie outside of stress shadows (e.g. F2-b). The along-strike migration of maximum slip at this stage may be important when trying to understand multi-fault ruptures that may occur on previously unrecognised faults, producing larger-than-expected earthquakes (e.g. Wesnousky, 1986; Leeder et al., 1991; Goldsworthy and Jackson, 2000; Gupta and Scholz, 2000; Hamling et al., 2017). Our results suggest that interactions between faults can be better understood through changes in fault geometry as an array evolves; this may allow for better predictability of earthquake recurrences in seismic hazard analysis, where a somewhat random Poisson-based process may be used (e.g. Reiter, 1990; Main, 1996; Mildon et al., 2019; Sgambato et al., 2020).

Fault growth trajectory using throw-length relationships

Figure 10 shows our new fault throw-length data for all 150 faults mapped in the Thebe fault array, relative to previously collected D-L data. Note that, in this plot, we have converted our throw data in ms TWT to displacement in metres, using an average dip of 60° and borehole-derived time-depth relationships (see section 3.1). On a log-log scale, our data approximately follow a linear trend (i.e. $n = 1$) across almost three orders of magnitude; this is similar to other global D-L scaling relationships for normal faults (e.g. Watterson, 1986; Walsh and Watterson, 1988; Marrett and Allmendinger, 1991; Cowie and Scholz, 1992) (Fig 10). Our data are coloured by dip direction; blue-coloured faults are broadly east-dipping and red-coloured faults are broadly west-dipping (see Fig 7). We observe that, whereas all faults abide by a broadly similar linear scaling relationship ($n = 1$), the major west-dipping (red-coloured) faults are presently somewhat 'over-displaced' ($c \sim 0.1$) relative to the smaller, antithetic, east-dipping faults ($c \sim 0.01$) (Fig 10). Most of the over-displaced faults are abandoned splays, left behind in the hanging walls of fault systems after relay breaching and segment linkage. These faults exhibit very short trace lengths but high throws. In contrast to over-displacement, under-displaced faults may be indicative of interpreting faults as *systems* instead of *segments*. For example, one fault segment F3-a exhibits a displacement-length ratio of 0.06, but the entire fault system in which it is contained (i.e. F3) is 46 km long and has a throw of 656 ms TWT (c. 858 m in displacement; Fig 8a). This gives a lower D-L ratio of 0.02 (Fig 10), demonstrating that D-L (and T-L) ratios are higher for individual fault segments than systems, although both still plot within the scatter observed in global range D-L data (Fig 10). Similar observations are noted by Peacock and Sanderson (1991) and Roberts and Michetti (2004), highlighting how mixing the analysis of fault segments (e.g. Meyer et al., 2002; Roberts et al., 2004) and/or fault systems (e.g. McLeod et al., 2000) may explain the range of scatter already seen in D-L profiles.

Fault length and displacement measurements for the present-day fault array (Fig 8a), coupled with the reconstructed fault array at c. 33% of the total rift duration (Fig 8b), allow us to define how D-L relationships have changed over the last c. 67% (57 Myr) of rift history. Our time-constrained displacement-length relationships reveal either: i) a vertical growth line, indicating that the fault accumulated displacement without lengthening (i.e. the constant fault growth model; Walsh et al., 2003; Nicol et al., 2005; Jackson and Rotevatn, 2013), or; ii) a static point, indicating that the faults was inactive during the last c. 67% of rifting (Figure 10 inset). Typically, faults that were inactive were the east-dipping antithetic faults that did not slip post-180 Ma and thus remained 'under-displaced' (Fig 10). Because all the major and minor fault systems dip westward and eastward, respectively, the structures onto which strain was eventually localised must have been set early in rift history (i.e. as early as the first c. 8% of the total rift duration). This may be attributed to positive stress feedback processes occurring during early array development, whereby shear stress reduction or 'stress shadow zones' inhibit fault growth and the nucleation of new cracks (e.g. Hu and Evans, 1989; Ackermann and Schlische, 1997; Cowie, 1998), and optimally positioned faults form and slip (i.e. faults with across-strike spacing of 12-14 km). Early establishment of the near-final fault lengths reinforces the suggestion that lateral tips of faults are effectively pinned by stress interactions with neighbouring faults (e.g. Burgmann et al., 1994; Willemse et al., 1996; Gupta and Scholz, 2000; Contreras, 2000). We propose that distributed faulting, principally characterized by fault lengthening, occurs until a given rock volume is 'strain saturated', as predicted by numerical and physical models (e.g. Cowie and Scholz 1992b; Cowie et al., 1995; Wu and Pollard, 1995; Ackermann et al., 2001).

Our observation that minor (E- dipping) faults either die early (where blue coloured faults are static points; Fig 10), or grow and still appear relatively under-displaced (where blue faults have a vertical trajectory that is relatively under-displaced; Fig 10) relative to larger faults onto which strain is subsequently localised (with higher displacement of red faults; Fig 10), has only been revealed from studying a complete fault array. Considering our data spans nearly three orders of magnitude, and given that the 150 faults formed in broadly similar rock types in the same stress regime, this implies that some of the scatter seen in D-L plots may simply be related to fault maturity and not only from limitations inherent to data collection (e.g. Kim and Sanderson, 2005) and/or differences in rock type and stress regime (e.g. Cowie and Scholz, 1992; Gillespie et al., 1992; Scholz et al., 1993).

Our findings illustrate the importance of collecting data from entire fault arrays developed over large areas if we hope to determine how normal faults grow. Datasets that allow inspection of only a small part of the rift (e.g. small-scale field-based studies), or analysis of faults lacking growth strata, could produce D-L relationships that appear anomalous (i.e. relatively under- or over-displaced) simply due to fault maturity (i.e. the datasets sample only the very young or old faults). Taking the trendline of datasets may produce an exponent value *n* that may not be representative of geometrical fault scaling relationships. We suspect that this may be why the true value of *n* is contested (e.g. Watterson, 1988; Marrett and Allmendinger, 1991; Gillespie et al., 1992; Cowie and Scholz, 1992; Clark and Cox, 1995; Dawers and Anders, 1995; Soliva et al., 2005; Xu et al., 2006; Torabi et al., 2011). By studying complete fault arrays rather than individual fault systems, we can better understand how faults grow and how continental extension proceeds.

A model of strain accommodation as the continental lithosphere stretches: incorporating segment- and system-scale growth

Although our study demonstrates that during the last c. 67% of rifting faults either grew by displacement accumulation or became inactive, the magnitude of displacement accumulation (i.e. the vertical trajectory on D-L profiles) does not extend outside of the overall scatter observed in global D-L plots (where c ~ 0.001, Figure 10). This is important, given that recently proposed fault models (constant-length and hybrid) commonly present growth trajectories only very schematically on D-L plots (e.g. Childs et al., 2017; Rotevatn et al., 2019; Fig 2). Due to the lack of scale on each axes, the constant-length and hybrid models also lack geometric constraint, which D-L profiles provide (i.e. faults cannot, for example, exhibit trace lengths of 10 km with 1 m of displacement, as this would plot well below the lower trendline of D-L profiles). However, current literature has frequently superimposed the schematic model trajectories onto global D-L data, in turn implying that faults that grow (or grew) via the constant-length and hybrid model apparently lie well outside of the known D-L scaling relationships. We suspect that many observations from ancient (inactive) and modern (active) extensional settings that endorse the constant-length model (e.g. Meyer et al., 2002; Tvedt et al., 2016; Jackson et al., 2017; Rotevatn et al., 2019) infact still lie within the bounds of our proposed geometrical constraint, as our results from offshore Australia show (Figure 10).

We propose a new model for how fault systems grow within an array, where faults ultimately scale by a linear relationship in log-log space (n = 1), but grow by alternating periods of lengthening and localisation, thereby producing a more step-like growth trajectory in D-L space than previously proposed (Fig 11). First, faults initiate as numerous, isolated segments (Stage 1 in Fig 11; e.g. Gawthorpe and Leeder, 1993). Fault lengthening via segment linkage occurs until a small rock volume (e.g. a mechanical layer of rock, which could at the largest scale represent the seismogenic crust) is saturated with faults with relatively little displacement. These early faults appear ‘under-displaced’ when viewed on D-L plots (2; Fig 11). Once the rock volume is sufficiently saturated with fault trace lengths defining the overall pattern of the fault network, optimally positioned faults (i.e. those that receive positive stress feedback from adjacent structures) then accrue displacement, whereas faults in stress shadow zones remain inactive and ultimately die (3; Fig 11). This phase of fault localisation and displacement accumulation produces a vertical growth trajectory on D-L plots, where active faults move vertically up until the upper scaling limit (approximately where c = 0.1). Fault that are not optimally positioned become inactive faults and die along the vertical trajectory, leaving a vertical spread of points. At this point, stress feedback mechanisms cause the fault array to be fully mechanically interacting, essentially inhibiting further fault interaction and growth. To further accommodate strain, the considered rock volume and the overall scale *increases* (from stage 3 to 4; fig 11). During this time the largest fault systems can mechanically interact (e.g. Ackermann et al 2001), acting again as isolated segments during the 'initiation' stage (4; Fig 11). These faults then lengthen, predominantly by segment linkage (5; Fig 11), and then strain localises onto optimally spaced zones, producing more widely spaced major faults (i.e. red fault segment; Fig 11). Faults located in stress shadow zones become inactive, appearing relatively under-displaced in D-L space (i.e. the green segment; Fig 11).

Our model includes aspects of the isolated and constant-length fault models. This is important because in the absence of data that truly constrains the temporal evolution of fault arrays and their constituent segments and systems, faults may appear to follow a sloping, linear trajectory, thereby endorsing the isolated model. The hybrid and constant-length models are also supported given that the final increment of fault growth, which in our study accounts for at least c. 67% of the rift history, is defined solely by displacement accumulation. Our fault growth model builds on this premise, however, by considering that faults systems interact as part of an array and are not kinematically or mechanically isolated (Fig 11).

Our suggested model inevitably leads to a lot of scatter in D-L profiles from the onset of extension, with this outcome indicating that the natural variability in D-L relationships may be an even bigger consequence of fault growth than previously suggested (e.g. Peacock and Sanderson 1991; Cartwright et al., 1995; Peacock and Sanderson, 1996). We suggest that the 'inflection point' between fault lengthening and displacement accumulation, bounded at D-L scaling trendlines (c, Fig 11), is controlled by the physical (e.g. mechanical strength, effective elastic thickness) characteristics of the region undergoing strain and, more specially, relates to layer thickness (cf. Ackermann et al., 2002) and areal extent, as this determines a 'saturation' point of fault lengths and displacements. Studies proposing a linear correlation between layer thickness and fault spacing are consistent with our updated model of fault growth, as this this relationship is largely driven by stress feedback mechanisms (Soliva and Benedicto, 2005; Soliva et al., 2006). Due to many natural mechanical heterogeneities in the subsurface, the 'inflection' transition may occur at any point in scale and account for the more subtle changes in growth trajectory path variability that may be lost in log-log space (Rotevatn et al., 2019). Further decrypting the 'natural' variability of global D-L plots by unravelling fault growth trajectories may allow us to better predict certain structural and mechanical properties, such as crustal thickness or mechanically confined layers in data-poor regions.

From our model, we are able to characterise the scaling properties and consider the growth stage of active and ancient, natural fault arrays. Fault populations that sit near the lower D-L boundary, where $c = 0.01$, exhibit distributed faulting, are seen in the Central Afar and on the Asal Ghoubbet faults in East Africa ($c \sim 0.012$ in Manghietti et al., 2015). In contrast, fault populations that lie closer to the upper D/L boundary ($c = 0.1$) may be characterised by more localised faulting, similar to that seen in fault populations imaged in seismic reflection data (e.g.

northern North Sea; McLeod et al., 2000, NW Shelf of Australia; Black et al., 2017). 3D seismic reflection surveys will often image now-inactive, ancient rifts that have proceeded through a phase of strain localisation. Therefore, typical fault system-scale studies may only capture the most mature faults that have accrued the largest amounts of displacement, potentially leading to an erroneous endorsement of the constant-length model. Conversely, studies from active rifts may be biased toward fault populations with lower c values, as immature faults in their early phase of development may be more readily captured by these datasets.

Resolving whether length establishment occurs within, for example, a few tens of thousands to a few million years is difficult with seismic reflection data from ancient rifts, given that the limited spatial and temporal resolution of seismic data at depth; it may thus be difficult to learn more about the fault lengthening stage from solely the kinematic analysis of seismic reflection data that image ancient basins. We suggest that future studies should focus on active, over-filled, shallowly buried (and thus seismically well-imaged) rifts (e.g. the Whakatane rift, New Zealand; Taylor et al., 2004), but 3D seismic data rather than grids of 2D data will really be required. Additionally, numerical and physical models may be able to test our hypothesis by constraining fault growth through global scaling relationships to investigate the inflection point of fault growth trajectories observed in D-L space.

6. CONCLUSIONS

- The timescales over which a fault array evolves have previously not been well constrained, due to a lack of dynamic, kinematic data.

- To fill this gap, we studied an extensive fault array (1200 km^2) in the Exmouth Plateau, NW Australia and characterised 150 seismically resolvable faults using displacement-length relationships.
- Isochron maps reveal that within the earliest resolvable slip increment of 7.2 Myrs (out of an overall duration of 85.5 Myrs) the majority of fault lengths have already been established.
- Fault displacement backstripping to 28.5 Myrs (33% of total rift duration) shows that the fault array was characterised with distributed faulting. Backstripping reveals along-strike slip migration through time to produce symmetric fault systems. Throw minima suggest previous segmentation and relay breaching.
- Our results allow us to view the last growth trajectory (representing the last 67% of total rift duration) on D-L plots. Faults undergo varying amounts of displacement accrual (i.e. the constant length model). Less (to no) displacement is accrued on faults in stress shadow zones.
- We propose that fault length and displacement scale linearly ($n = 1$) but grow via alternating phases of lengthening and displacement accrual. Our model is largely based on stress feedback mechanisms driven by layer/crustal thickness, which produce 'inflection' points in D-L space.
- Inactive faults located in stress shadow zones contribute towards the large amount of global displacement-length scatter due to differences in fault maturity. As the scatter may be inherent to fault growth, D-L relationships may help us to differentiate fault characteristics in ancient and modern rifts.

ACKNOWLEDGEMENTS

This manuscript contains work conducted during a PhD study undertaken as part of the Natural Environment Research Council (NERC) Centre for Doctoral Training (CDT) in Oil & Gas [NE/R01051X/1]. We are grateful for the provision of publicly accessible subsurface data by Geoscience Australia – the Thebe 3D dataset can be downloaded from the NOPIMS data repository website: https://nopims.dmp.wa.gov.au/nopims. We thank Geoteric for downloading and transferring the dataset for us, as well as providing access to their software. Schlumberger are thanked for the donation of Petrel software licences.

FIGURE CAPTIONS

Figure 1. Fault array evolution, modified after Gawthorpe and Leeder, (2000). Faults grow from an initiation stage (A) with isolated, short (20-10 km) and low-displacement fault segments into a period of interaction and linkage (B), and finally strain localises onto a few long (>10 km), high displacement 'through-going' fault zones (C). Typically, studies investigating fault growth measure the geometry of fault systems when they have reached (C).

Figure 2. Global displacement-length (D-L) data of normal faults. D-L relationships are presented in log-log space, therefore the line of best fit results in the scaling exponent, n. Faults may grow via the isolated where increases in displacement and length occur sympathetically, producing the green growth trajectory; or the constant-length model where the final length is established early in slip history, prior to accumulation of significant displacement, producing the blue trajectory.

Figure 3. The location of our study area: (a) Location of the Thebe field seismic dataset within the Exmouth Plateau, North Carnarvon Basin, North West Shelf of Australia. Sub-basin boundaries are taken from Geoscience Australia. The main structural NE- trends in Fig 3b are

from Bilal et al. 2019; and (b) The main structural elements of the Thebe dataset. Major fault systems are labelled in colour, correlating to their respective throw-profiles in Figure 8. Minor faults are coloured in light grey. Wells Thebe-1 and Thebe-2 are shown.

Figure 4. Horizons and their respective formation ages. H1 and H10 are pre-rift and post-rift reflectors, whereas H2 – H9 define the syn-kinematic unit of the study area. H4, H5 and H6 do not contain biostratigraphic ages, therefore age is inferred through the assumption of constant sedimentation. Our different methodologies to understand rift evolution are resolved to different stages in time, which has been demonstrated on the right.

Figure 5. Cross section of inline 1524 (location shown on Figure 3b): (a) Without interpretation; and (b) With interpretation and annotation highlighting the main structural features of the overall study area.

Figure 6. Time-surface maps (ms TWT) showing the present day structure of the dataset. Faults at each successive interval are mapped using a variance attribute overlay for higher confidence.

Figure 7. Dip direction of the fault array. The rose diagram shows the average strike azimuth and dip direction per fault segment. The rose diagram is split into two halves, whereby the blue coloured faults are east dipping, and the red coloured faults are west dipping.

Figure 8. Throw length profiles (segments coloured by Fig 3b) and their map view throw distribution, for (a) The present day fault array, i.e. the final product of rift history; and (b) The reconstructed, backstripped fault array, where faults are backstripped to 28.5 Myrs (H4; Top Murat).

Figure 9. Isochron maps showing thickness changes between syn-depositional horizons. The syn-rift unit is divided into six, labelled as SU1-SU6.

Figure 10. Our results plotted against global displacement-length data in grey. Our data is coloured by the dip map (see Figure 7) whereby blue-coloured faults are east dipping, and red-coloured faults are red dipping. Our results were measured in throw, but we have converted our values into displacement by assuming an average dip of 60 (see supplementary table for raw values). The inset shows the last 67% of rift history, as we connect our present-day values of fault geometry with their respective backstripped values.

Figure 11. Our new proposed fault growth model, where the fault trajectory shows growth via alternating phases of fault lengthening (producing a near horizontal trajectory) and fault displacement (producing a near vertical trajectory). Stage 1, 2 and 3 are examples of initiation, linkage and localisation over a smaller region. Faults initiate as small numerous fault segments (1), then lengthen via segment linkage until the rock volume is sufficiently saturated, producing relatively under-displaced D-L values (2), displacement accrues on optimally located and spaced faults (3). Once the smaller region is saturated by fault lengths and displacement, the considered region increases, allowing the fault array to undergo initiation (4), lengthening (5) and localisation (6) again at a larger scale.

DATA AVAILABILITY STATEMENT

The data that support the findings of this study are available from the corresponding author upon reasonable request.

REFERENCES CITED

Allmendinger, R.W. and Zapata, T.R., 2000. The footwall ramp of the Subandean decollement, northernmost Argentina, from extended correlation of seismic reflection data. *Tectonophysics*, *321*(1), pp.37-55.

Anders, M.H. and Schlische, R.W., 1994. Overlapping faults, intrabasin highs, and the growth of normal faults. *The Journal of Geology*, *102*(2), pp.165-179.

Bailey, W.R., Walsh, J.J. and Manzocchi, T., 2005. Fault populations, strain distribution and basement fault reactivation in the East Pennines Coalfield, UK. *Journal of Structural Geology*, *27*(5), pp.913-928.

Baker, B.H., Mohr, P.A. and Williams, L.A.J., 1972. *Geology of the eastern rift system of Africa* (Vol. 136). Geological Society of America.

Barber, P.M., 1988. The Exmouth Plateau deep water frontier: a case history.

Bell, R.E., Jackson, C.A.L., Whipp, P.S. and Clements, B., 2014. Strain migration during multiphase extension: Observations from the northern North Sea. *Tectonics*, *33*(10), pp.1936-1963.

Bell, R.E., McNeill, L.C., Bull, J.M., Henstock, T.J., Collier, R.L. and Leeder, M.R., 2009. Fault architecture, basin structure and evolution of the Gulf of Corinth Rift, central Greece. *Basin Research*, *21*(6), pp.824-855.

Bilal, A., McClay, K. and Scarselli, N., 2018. Fault-scarp degradation in the central Exmouth Plateau, North West Shelf, Australia. *Geological Society, London, Special Publications*, *476*, pp.SP476-11.

Black, M., McCormack, K.D., Elders, C. and Robertson, D., 2017. Extensional fault evolution within the Exmouth Sub-basin, North West Shelf, Australia. *Marine and Petroleum Geology*, *85*, pp.301-315.

Bosworth, W., 1985. Geometry of propagating continental rifts. *Nature*, *316*(6029), p.625.

Cartwright, J.A., Trudgill, B.D. and Mansfield, C.S., 1995. Fault growth by segment linkage: an explanation for scatter in maximum displacement and trace length data from the Canyonlands Grabens of SE Utah. *Journal of Structural Geology*, *17*(9), pp.1319-1326.

Chapman, T.J. and Meneilly, A.W., 1991. The displacement patterns associated with a reverse-reactivated, normal growth fault. *Geological Society, London, Special Publications*, *56*(1), pp.183-191.

Childs, C., Manzocchi, T., Nicol, A., Walsh, J.J., Soden, A.M., Conneally, J.C. and Delogkos, E., 2017. The relationship between normal drag, relay ramp aspect ratio and fault zone structure. *Geological Society, London, Special Publications*, *439*(1), pp.355-372.

Childs, C., Nicol, A., Walsh, J.J. and Watterson, J., 2003. The growth and propagation of synsedimentary faults. *Journal of Structural geology*, *25*(4), pp.633-648.

Cladouhos, T.T. and Marrett, R., 1996. Are fault growth and linkage models consistent with power-law distributions of fault lengths?. *Journal of Structural Geology*, *18*(2-3), pp.281-293.

Collettini, C. and Barchi, M.R., 2002. A low-angle normal fault in the Umbria region (Central Italy): a mechanical model for the related microseismicity. *Tectonophysics*, *359*(1-2), pp.97-115.

Cowie, P.A. and Scholz, C.H., 1992. Physical explanation for the displacement-length relationship of faults using a post-yield fracture mechanics model. *Journal of Structural Geology*, *14*(10), pp.1133-1148.

Cowie, P.A., Gupta, S. and Dawers, N.H., 2000. Implications of fault array evolution for synrift depocentre development: insights from a numerical fault growth model. *Basin Research*, *12*(3-4), pp.241-261.

Dawers, N.H. and Underhill, J.R., 2000. The role of fault interaction and linkage in controlling synrift stratigraphic sequences: Late Jurassic, Statfjord East area, northern North Sea. *AAPG bulletin*, *84*(1), pp.45-64.

Driscoll, N.W. and Karner, G.D., 1998. Lower crustal extension across the Northern Carnarvon basin, Australia: Evidence for an eastward dipping detachment. *Journal of Geophysical Research: Solid Earth*, *103*(B3), pp.4975-4991.

Dutton, D.M. and Trudgill, B.D., 2009. Four-dimensional analysis of the Sembo relay system, offshore Angola: Implications for fault growth in salt-detached settings. *AAPG bulletin*, *93*(6), pp.763-794.

Estimates of strain due to brittle faulting: sampling of fault populations. *Journal of Structural Geology*, *13*(6), pp.735-738.*10*(3), pp.239-247.

Exon, N.F., Haq, B.U. and Von Rad, U., 1992. Exmouth Plateau revisited: scientific drilling and geological framework. In *Proceedings of the Ocean Drilling Program, Scientific Results* (Vol. 122, pp. 3-20). College Station, Tex: Ocean Drilling Program.

Gartrell, A.P., 2000. Rheological controls on extensional styles and the structural evolution of the Northern Carnarvon Basin, North West Shelf, Australia. *Australian Journal of Earth Sciences*, *47*(2), pp.231-244.

Gawthorpe, R.L. and Leeder, M.R., 2000. Tectono-sedimentary evolution of active extensional basins. *Basin Research*, *12*(3-4), pp.195-218.

Gawthorpe, R.L., Jackson, C.A.L., Young, M.J., Sharp, I.R., Moustafa, A.R. and Leppard, C.W., 2003. Normal fault growth, displacement localisation and the evolution of normal fault populations: the Hammam Faraun fault block, Suez rift, Egypt. *Journal of Structural Geology*, *25*(6), pp.883-895.

Gibbons, A.D., Barckhausen, U., Van Den Bogaard, P., Hoernle, K., Werner, R., Whittaker, J.M. and Müller, R.D., 2012. Constraining the Jurassic extent of Greater India: Tectonic evolution of the West Australian margin. *Geochemistry, Geophysics, Geosystems*, *13*(5).

Gillespie, P.A., Howard, C.B., Walsh, J.J. and Watterson, J., 1993. Measurement and characterisation of spatial distributions of fractures. *Tectonophysics*, *226*(1-4), pp.113-141.

Gupta, S., Cowie, P.A., Dawers, N.H. and Underhill, J.R., 1998. A mechanism to explain rift-basin subsidence and stratigraphic patterns through fault-array evolution. *Geology*, *26*(7), pp.595-598.

Gutenberg, B. and Richter, C.F., 1944. Frequency of earthquakes in California. *Bulletin of the Seismological Society of America*, *34*(4), pp.185-188.

Hamilton, W., 1987. Mesozoic geology and tectonics of the Big Maria Mountains region, southeastern California. *Mesozoic rocks of southern Arizona and adjacent areas: Arizona Geological Society Digest*, *18*, pp.33-47.

Heine, C. and Müller, R.D., 2005. Late Jurassic rifting along the Australian North West Shelf: margin geometry and spreading ridge configuration. *Australian Journal of Earth Sciences*, *52*(1), pp.27-39.

Hocking, R.M. and Preston, W.A., 1998. Western Australia: Phanerozoic geology and mineral resources. *AGSO Journal of Australian Geology and Geophysics*, *17*, pp.245-260.

Jablonski, D., 1997. Recent advances in the sequence stratigraphy of the Triassic to Lower Cretaceous succession in the Northern Carnarvon Basin, Australia. *The APPEA Journal*, *37*(1), pp.429-454.

Jackson, C.A.L. and Rotevatn, A., 2013. 3D seismic analysis of the structure and evolution of a salt-influenced normal fault zone: a test of competing fault growth models. *Journal of*

Structural Geology, *54*, pp.215-234.

Jackson, C.A.L. and Rotevatn, A., 2013. 3D seismic analysis of the structure and evolution of a salt-influenced normal fault zone: a test of competing fault growth models. *Journal of Structural Geology*, *54*, pp.215-234.

Jackson, C.A.L., Bell, R.E., Rotevatn, A. and Tvedt, A.B., 2017. Techniques to determine the kinematics of synsedimentary normal faults and implications for fault growth models. *Geological Society, London, Special Publications*, *439*(1), pp.187-217.

Kanamori, H. and Anderson, D.L., 1975. Theoretical basis of some empirical relations in seismology. *Bulletin of the seismological society of America*, *65*(5), pp.1073-1095.

King, G.C. and Sammis, C.G., 1992. The mechanisms of finite brittle strain. *Pure and Applied Geophysics*, *138*(4), pp.611-640.

Kostrov, V.V., 1974. Seismic moment and energy of earthquakes, and seismic flow of rock. *Izv. Acad. Sci. USSR Phys. Solid Earth*, *1*, pp.23-44.

Leeder, M.R. and Jackson, J.A., 1993. The interaction between normal faulting and drainage in active extensional basins, with examples from the western United States and central Greece. *Basin research*, *5*(2), pp.79-102.

Logatchev, N.A. and Zorin, Y.A., 1992. Baikal rift zone: structure and geodynamics. *Tectonophysics*, *208*(1-3), pp.273-286.

Long, J.J. and Imber, J., 2010. Geometrically coherent continuous deformation in the volume surrounding a seismically imaged normal fault-array. *Journal of Structural Geology*, *32*(2), pp.222-234.

Longley, I.M., Buessenschuett, C., Clydsdale, L., Cubitt, C.J., Davis, R.C., Johnson, M.K., Marshall, N.M., Murray, A.P., Somerville, R., Spry, T.B. and Thompson, N.B., 2002, October. The North West Shelf of Australia—a Woodside perspective. In *The Sedimentary Basins of Western Australia 3: Proceedings of the Petroleum Exploration Society of Australia Symposium, Perth* (pp. 27-88). Perth: Pet. Explor. Soc. of Aust..

Manzocchi, T., Walsh, J.J. and Bailey, W.R., 2009. Population scaling biases in map samples of power-law fault systems. *Journal of Structural Geology*, *31*(12), pp.1612-1626.

Marrett, R. and Allmendinger, R.W., 1990. Kinematic analysis of fault-slip data. *Journal of structural geology*, *12*(8), pp.973-986.

McCormack, K.D. and McClay, K., 2013, August. Structural architecture of the gorgon platform, North West Shelf, Australia. In *The Sedimentary Basins of Western Australia IV: Proceedings of the Petroleum Exploration Society of Australia Symposium, Perth, WA* (pp. 1-24).

McLeod, A.E., Dawers*, N.H. and Underhill, J.R., 2000. The propagation and linkage of normal faults: insights from the Strathspey–Brent–Statfjord fault array, northern North Sea. *Basin Research*, *12*(3-4), pp.263-284.

Metcalfe, I., 2013. Gondwana dispersion and Asian accretion: Tectonic and palaeogeographic evolution of eastern Tethys. *Journal of Asian Earth Sciences*, *66*, pp.1-33.

Meyer, V., Nicol, A., Childs, C., Walsh, J.J. and Watterson, J., 2002. Progressive localisation of strain during the evolution of a normal fault population. *Journal of Structural Geology*, *24*(8), pp.1215-1231.

Molnar, P. and Chen, W.P., 1983. Focal depths and fault plane solutions of earthquakes under the Tibetan plateau. *Journal of Geophysical Research: Solid Earth*, *88*(B2), pp.1180-1196.

Morley, C.K., 2002. A tectonic model for the Tertiary evolution of strike–slip faults and rift basins in SE Asia. *Tectonophysics*, *347*(4), pp.189-215.

Nicol, A., Walsh, J., Berryman, K. and Nodder, S., 2005. Growth of a normal fault by the accumulation of slip over millions of years. *Journal of Structural Geology*, *27*(2), pp.327-342.

Peacock, D.C.P. and Sanderson, D.J., 1991. Displacements, segment linkage and relay ramps in normal fault zones. *Journal of Structural Geology*, *13*(6), pp.721-733.

Petersen, K., Clausen, O.R. and Korstgård, J.A., 1992. Evolution of a salt-related listric growth fault near the D-1 well, block 5605, Danish North Sea: displacement history and salt kinematics. *Journal of Structural Geology*, *14*(5), pp.565-577.

Pryer, L.L., Romine, K.K., Loutit, T.S. and Barnes, R.G., 2002. Carnarvon basin architecture and structure defined by the integration of mineral and petroleum exploration tools and techniques. *The APPEA Journal*, *42*(1), pp.287-309.

Rotevatn, A., Jackson, C.A.L., Tvedt, A.B., Bell, R.E. and Blækkan, I., 2019. How do normal faults grow?. *Journal of Structural Geology*, *125*, pp.174-184.

Rowan, M.G., Hart, B.S., Nelson, S., Flemings, P.B. and Trudgill, B.D., 1998. Three-dimensional geometry and evolution of a salt-related growth-fault array: Eugene Island 330 field, offshore Louisiana, Gulf of Mexico. *Marine and petroleum geology*, *15*(4), pp.309-328.

Schlische, R.W., Young, S.S., Ackermann, R.V. and Gupta, A., 1996. Geometry and scaling relations of a population of very small rift-related normal faults. *Geology*, *24*(8), pp.683-686.

Scholz, C.H., Dawers, N.H., Yu, J.Z., Anders, M.H. and Cowie, P.A., 1993. Fault growth and fault scaling laws: preliminary results. *Journal of Geophysical Research: Solid Earth*, *98*(B12), pp.21951-21961.

Seyitoğlu, G. and Scott, B.C., 1996. Age of the Alaşehir graben (west Turkey) and its tectonic implications. *Geological Journal*, *31*(1), pp.1-11.

Stagg, H.M.J. and Colwell, J.B., 1994. The structural foundations of the Northern Carnarvon Basin.

Thorsen, C.E., 1963. Age of growth faulting in southeast Louisiana.

Walsh, J.J. and Watterson, J., 1988. Analysis of the relationship between displacements and dimensions of faults. *Journal of Structural geology*, Marrett, R. and Allmendinger, R.W., 1991.

Walsh, J.J., Childs, C., Imber, J., Manzocchi, T., Watterson, J. and Nell, P.A.R., 2003. Strain localisation and population changes during fault system growth within the Inner Moray Firth, Northern North Sea. *Journal of Structural Geology*, *25*(2), pp.307-315.

Walsh, J.J., Nicol, A. and Childs, C., 2002. An alternative model for the growth of faults. *Journal of Structural Geology*, *24*(11), pp.1669-1675.

Watterson, J., 1986. Fault dimensions, displacements and growth. *Pure and Applied Geophysics*, *124*(1-2), pp.365-373.

Whipp, P.S., Jackson, C.A.L., Gawthorpe, R.L., Dreyer, T. and Quinn, D., 2014. Normal fault array evolution above a reactivated rift fabric; a subsurface example from the northern Horda Platform, Norwegian North Sea. *Basin Research*, *26*(4), pp.523-549.

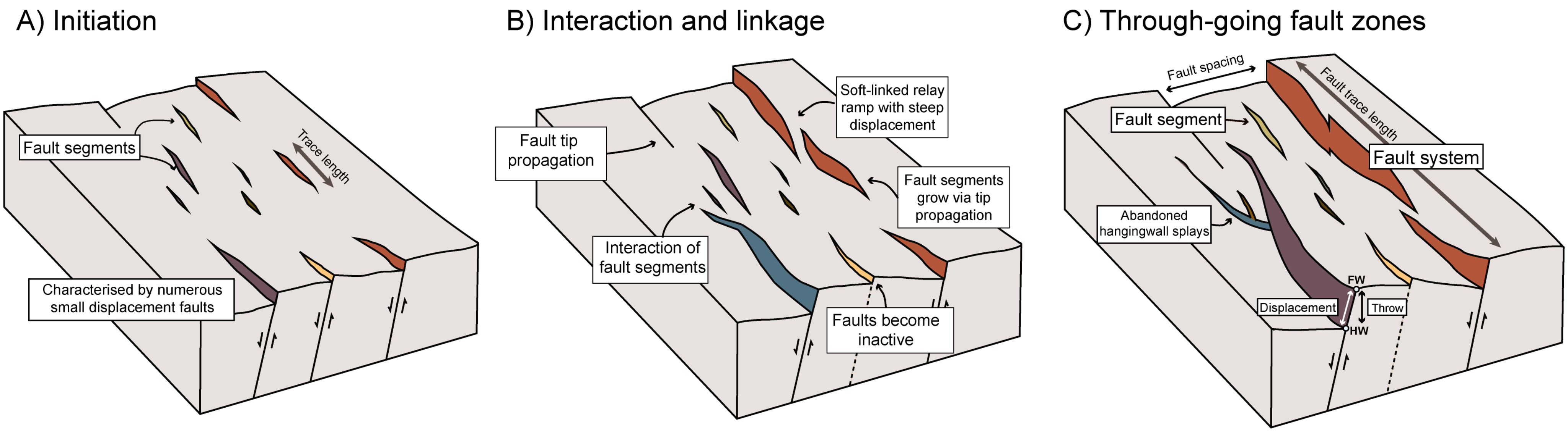

Figure 1. Fault array evolution, modified after Gawthorpe and Leeder (2000). Faults grow from an initiation stage (A) with isolated, short (20-10 km) and low-displacement fault segments into a period of interaction and linkage (B), and finally strain localises onto a few long (>10 km), high displacement 'through-going' fault zones (C). Typically, studies investigating fault growth measure the geometry of fault systems when they have reached (C).

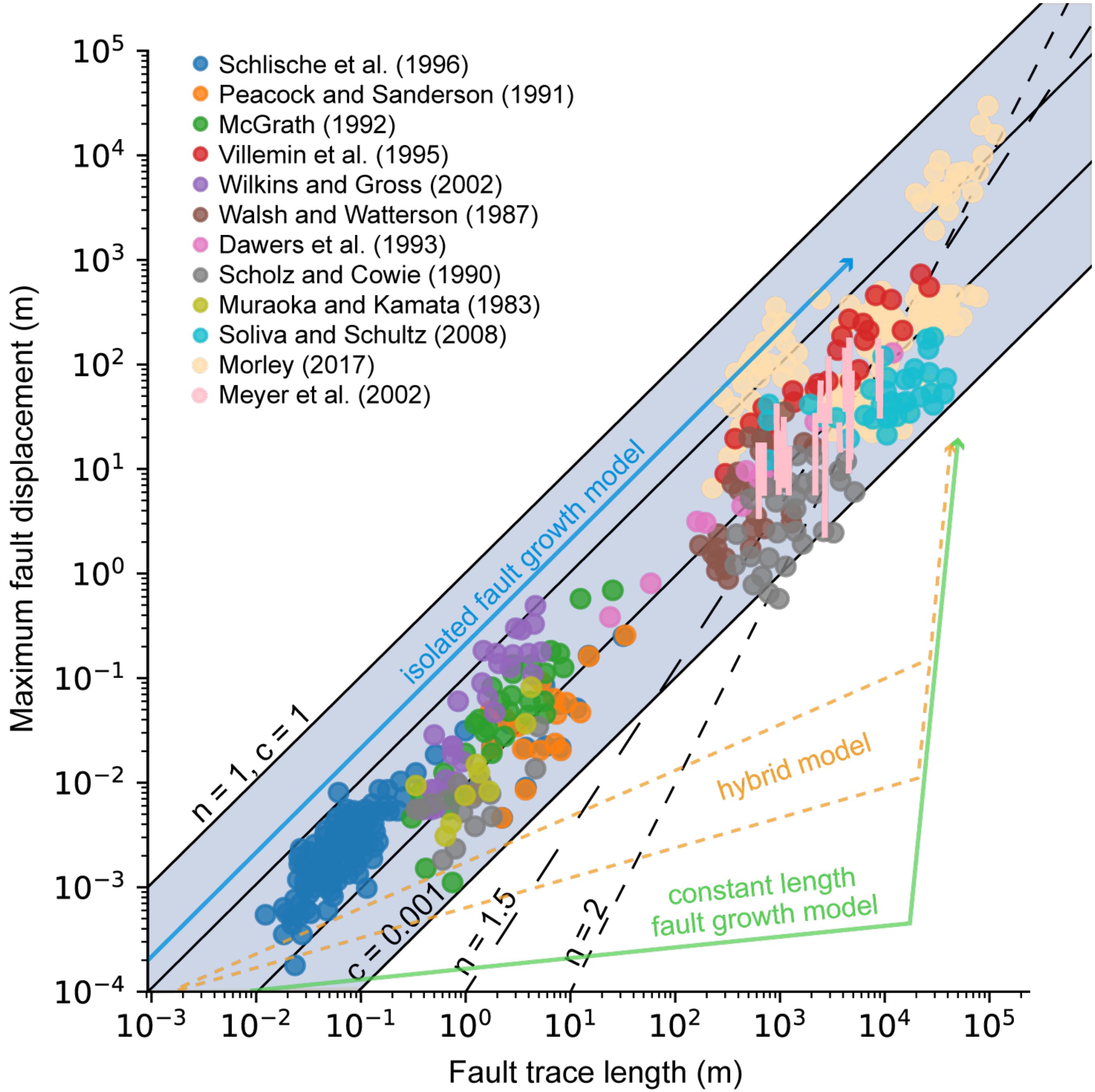

Figure 2. Global displacement-length (D-L) data of normal faults. D-L relationships are presented in log-log space, therefore the line of best fit results in the scaling exponent, n. Faults may grow via the isolated model where increases in displacement and length occur sympathetically, producing the blue growth trajectory; or the constant-length model where the final length is established early in slip history, prior to accumulation of significant displacement, producing the green trajectory.

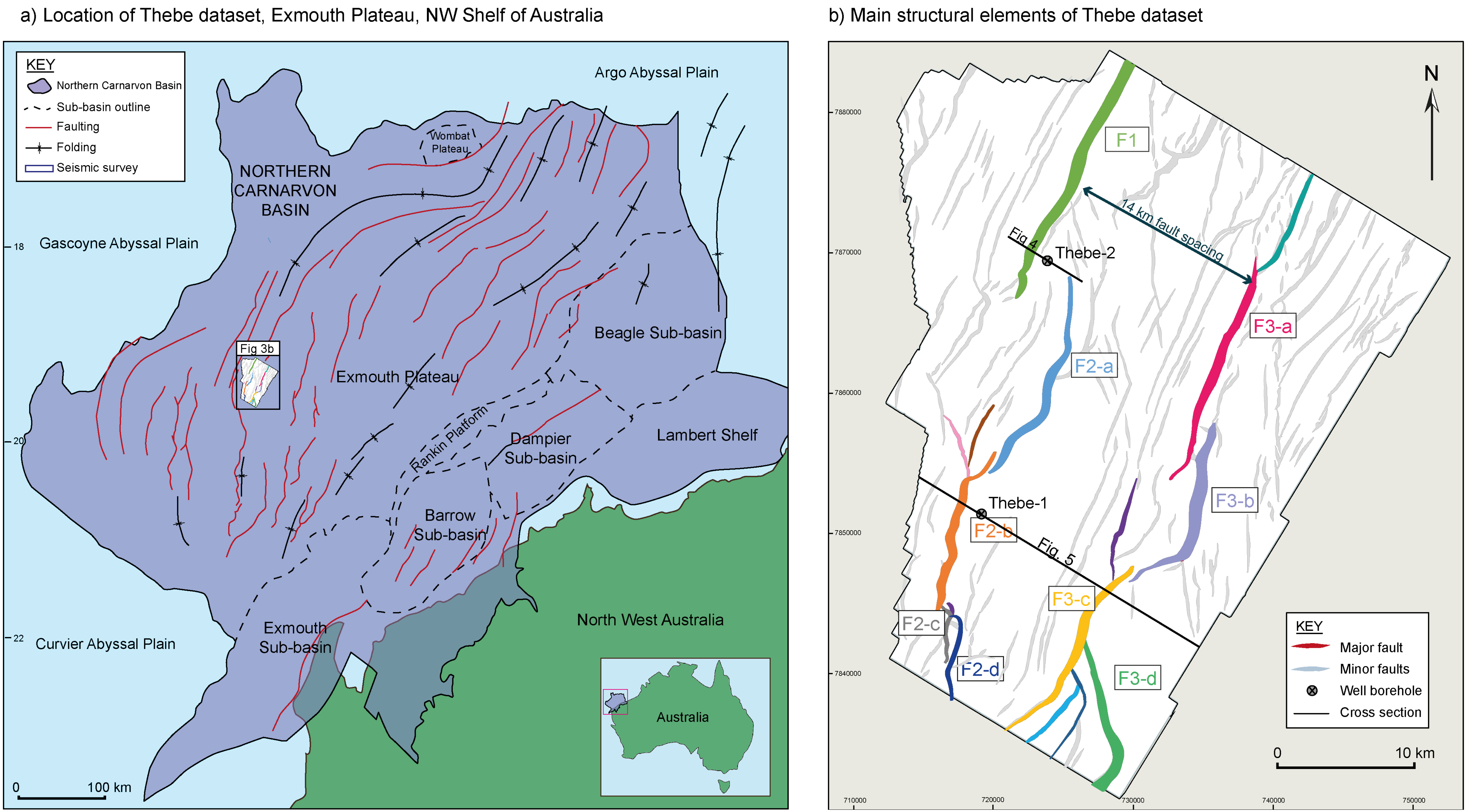

Figure 3. The location of our study area: (a) Location of the Thebe field seismic dataset within the Exmouth Plateau, North Carnarvon Basin, North West Shelf of Australia. Sub-basin boundaries are taken from Geoscience Australia. The main structural NE- trends in Fig 3b are from Bilal et al., (2019); and (b) The main structural elements of the Thebe dataset. Major fault systems are labelled in colour, correlating to their respective throw-profiles in Figure 8. Minor faults are coloured in light grey. Wells Thebe-1 and Thebe-2 are shown.

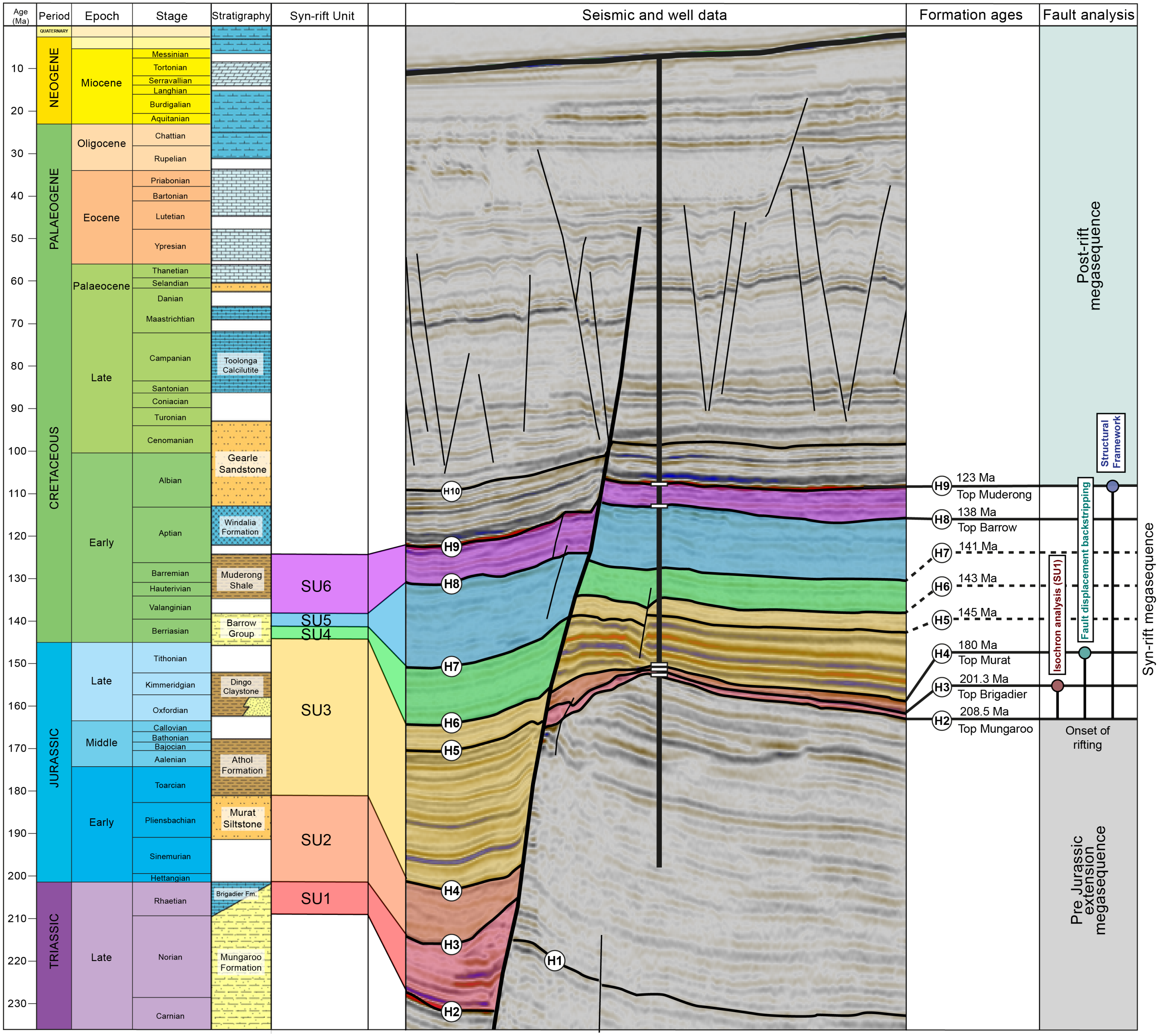

Figure 4. Horizons and their respective formation ages. H1 and H10 are pre-rift and post-rift reflectors, whereas H2 – H9 define the syn-kinematic unit of the study area. H4, H5 and H6 do not contain biostratigraphic ages, therefore age is inferred through the assumption of constant sedimentation. Various methodologies used to understand rift evolution are resolved to different stages in time, which has been demonstrated on the right.

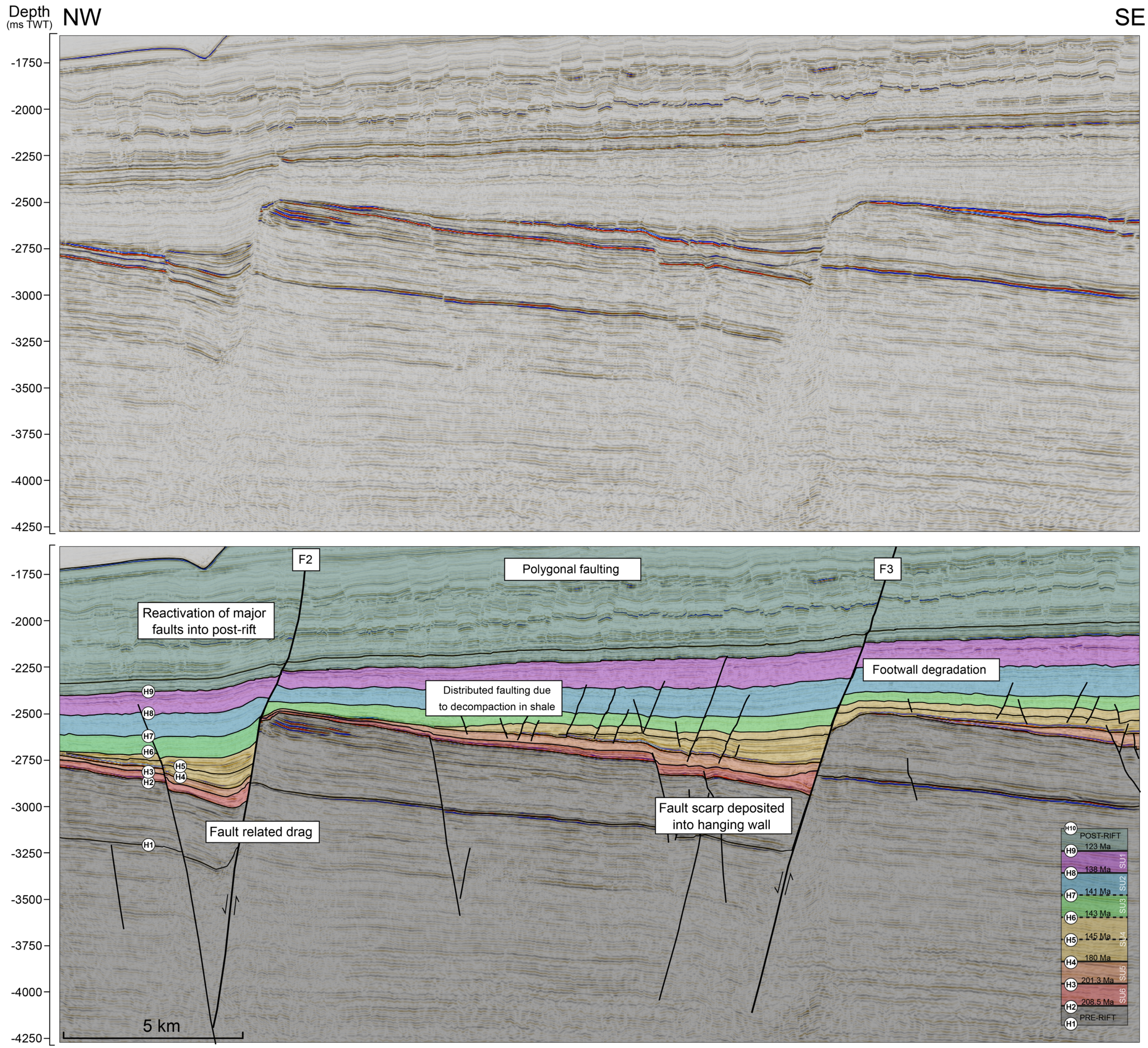

Figure 5. Cross section of inline 1524 - location shown on Figure 3b: (a) Without interpretation; and (b) With interpretation and annotation highlighting the main structural features of the overall study area.

Figure 6. Time-surface maps (ms TWT) showing the present day structure of the dataset. Faults at each successive interval are mapped using a variance attribute overlay for higher confidence.

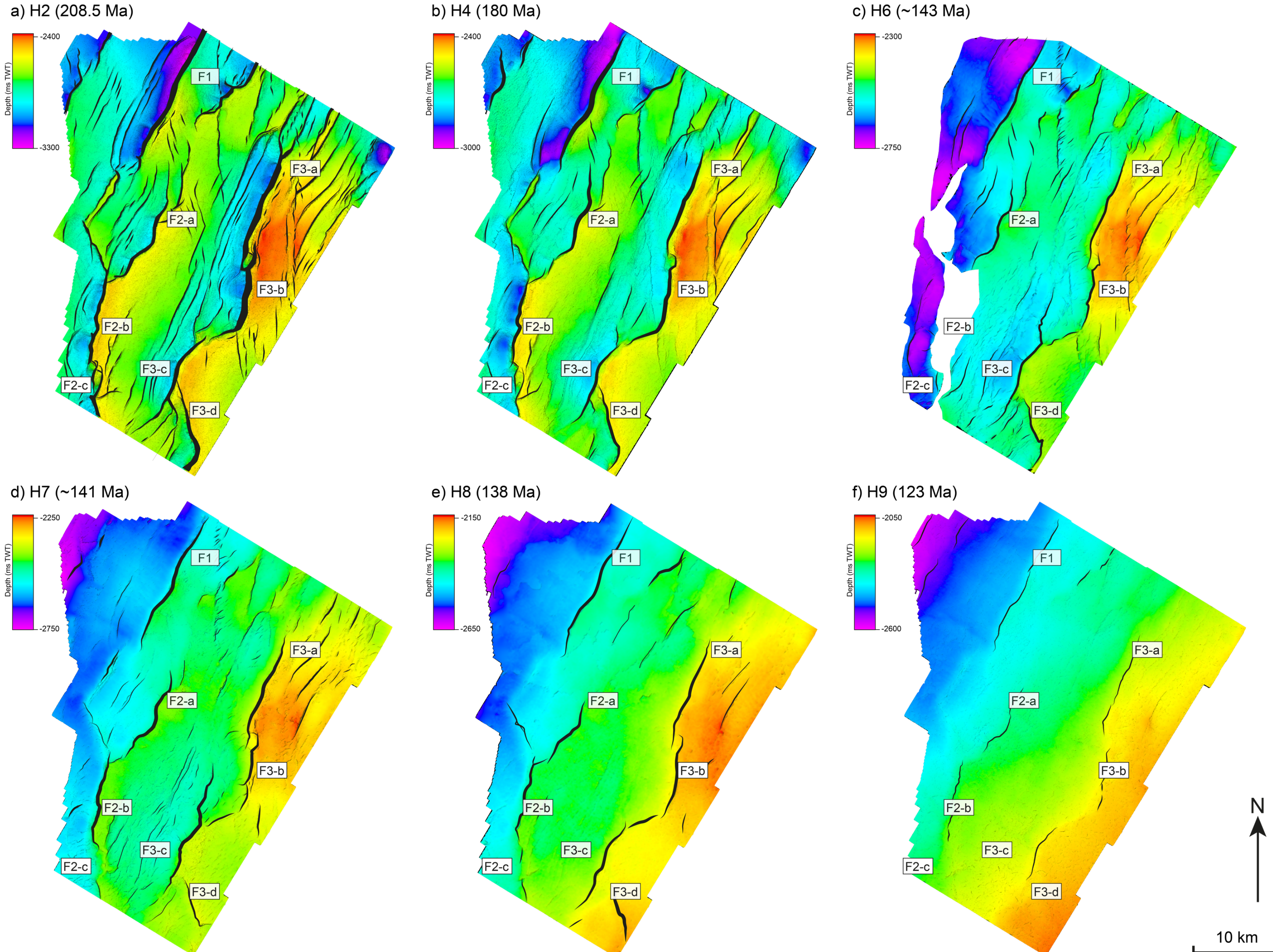

Figure 7. Dip direction of the fault array. The rose diagram shows the average strike azimuth and dip direction per fault segment. The rose diagram is split into two halves, whereby the blue coloured faults are east dipping, and the red coloured faults are west dipping.

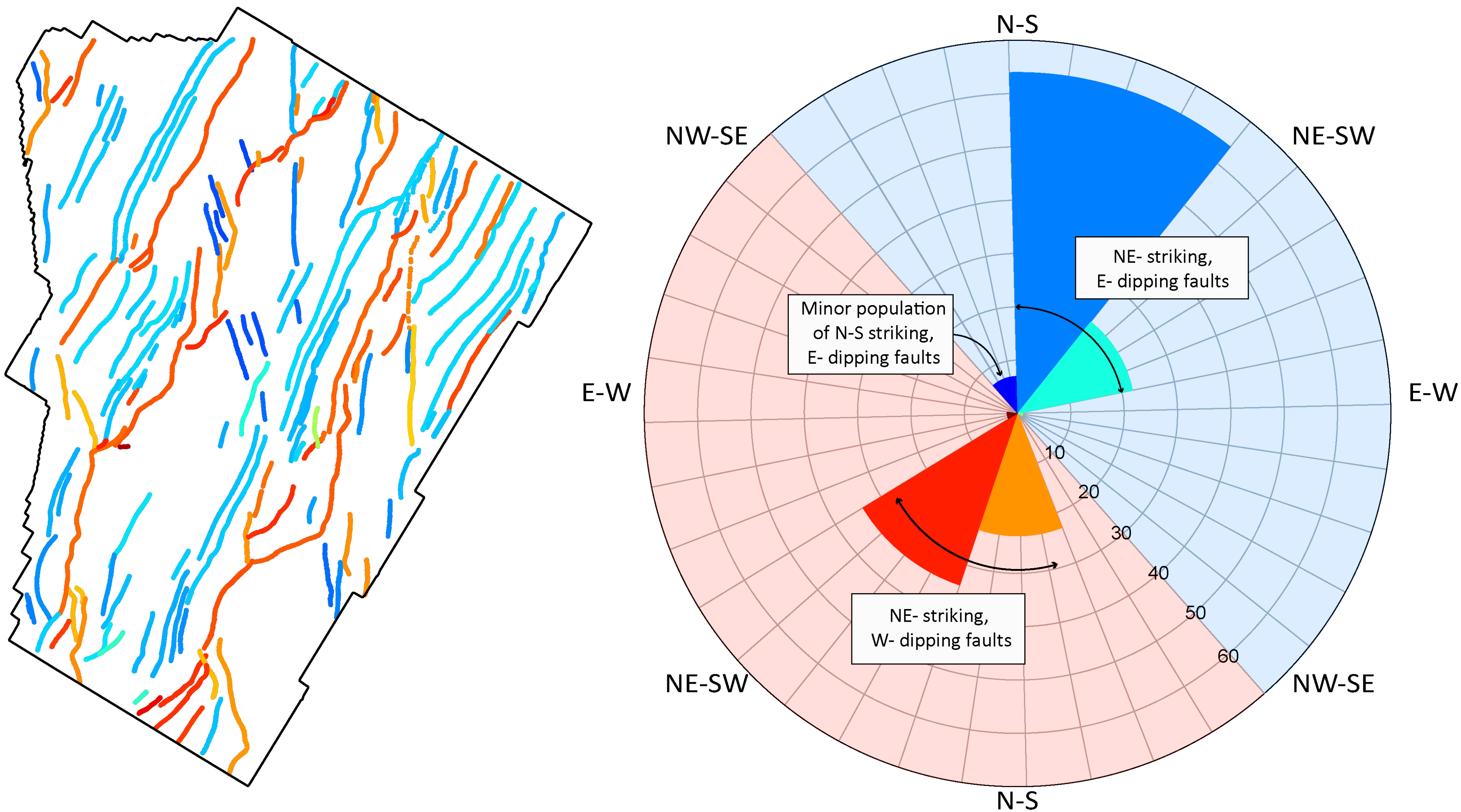

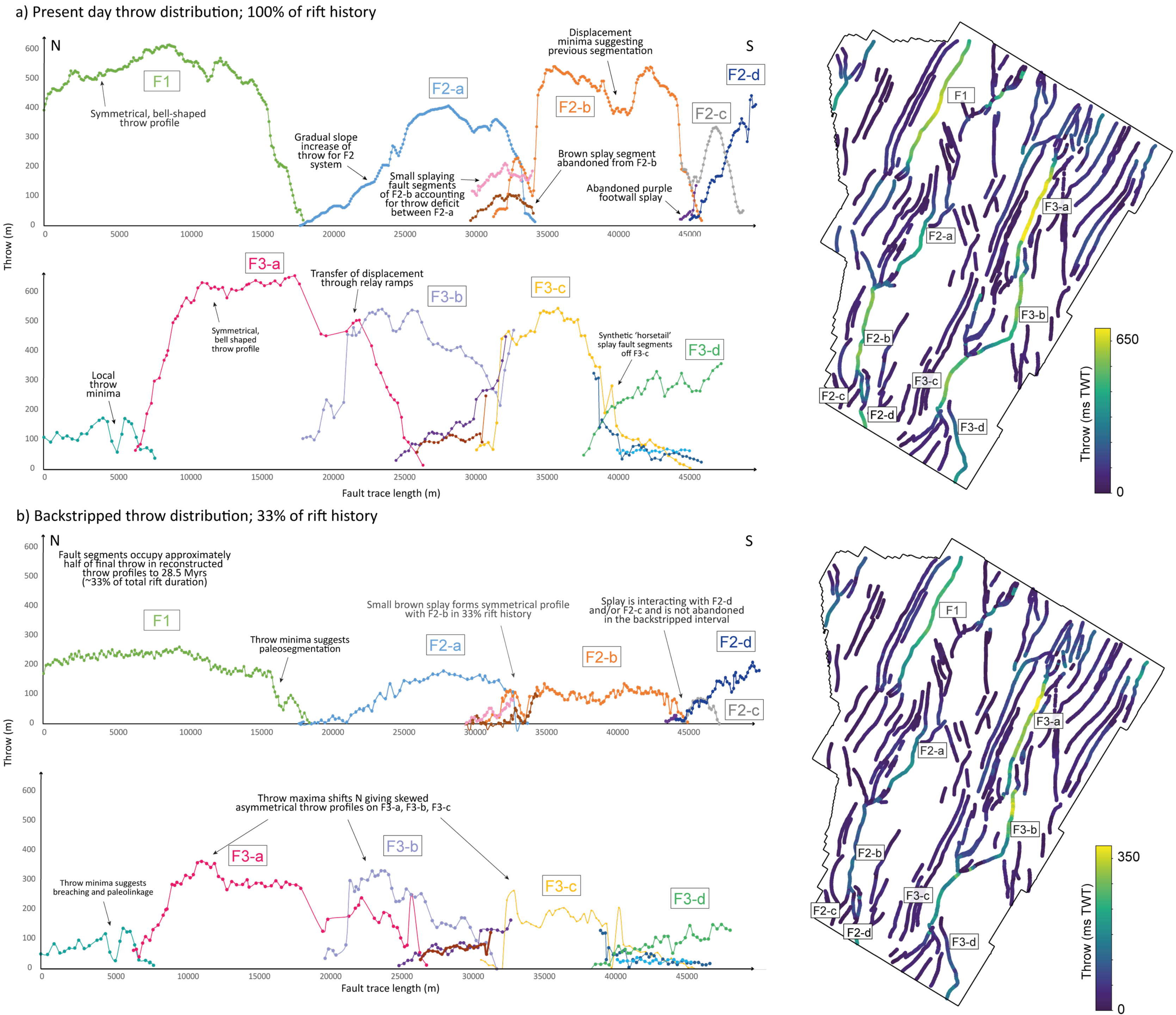

Figure 8. Throw length profiles (where fault segments are coloured by Fig 3b) with a map view of throw distribution: (a) The present day fault array, i.e. the final product of rift history; and (b) The reconstructed, backstripped fault array, where faults are backstripped to 28.5 Myrs (H4; Top Murat).

Figure 9. Isochron maps showing thickness changes between syn-depositional horizons. The syn-rift unit is divided into six, labelled as SU1-SU6.

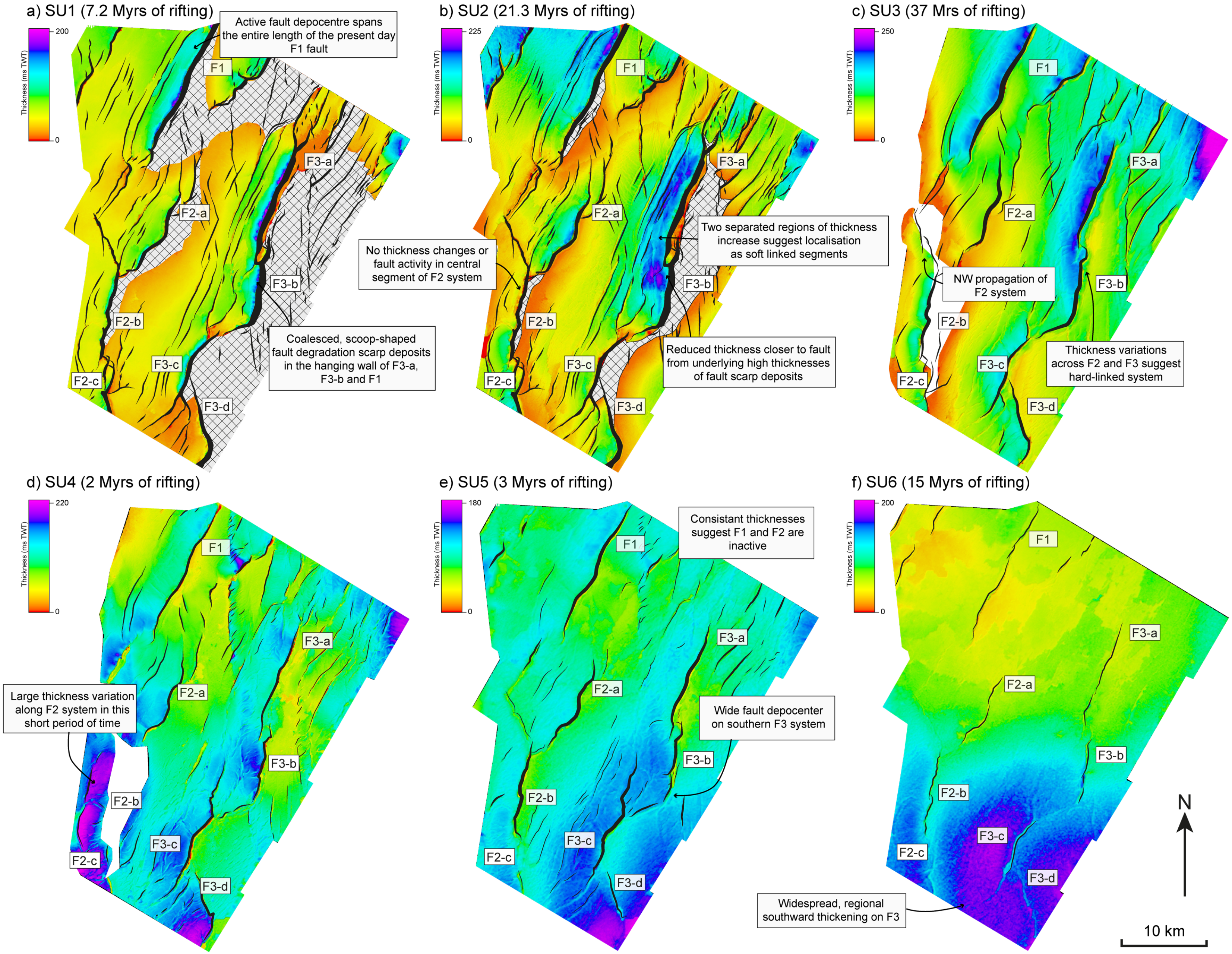

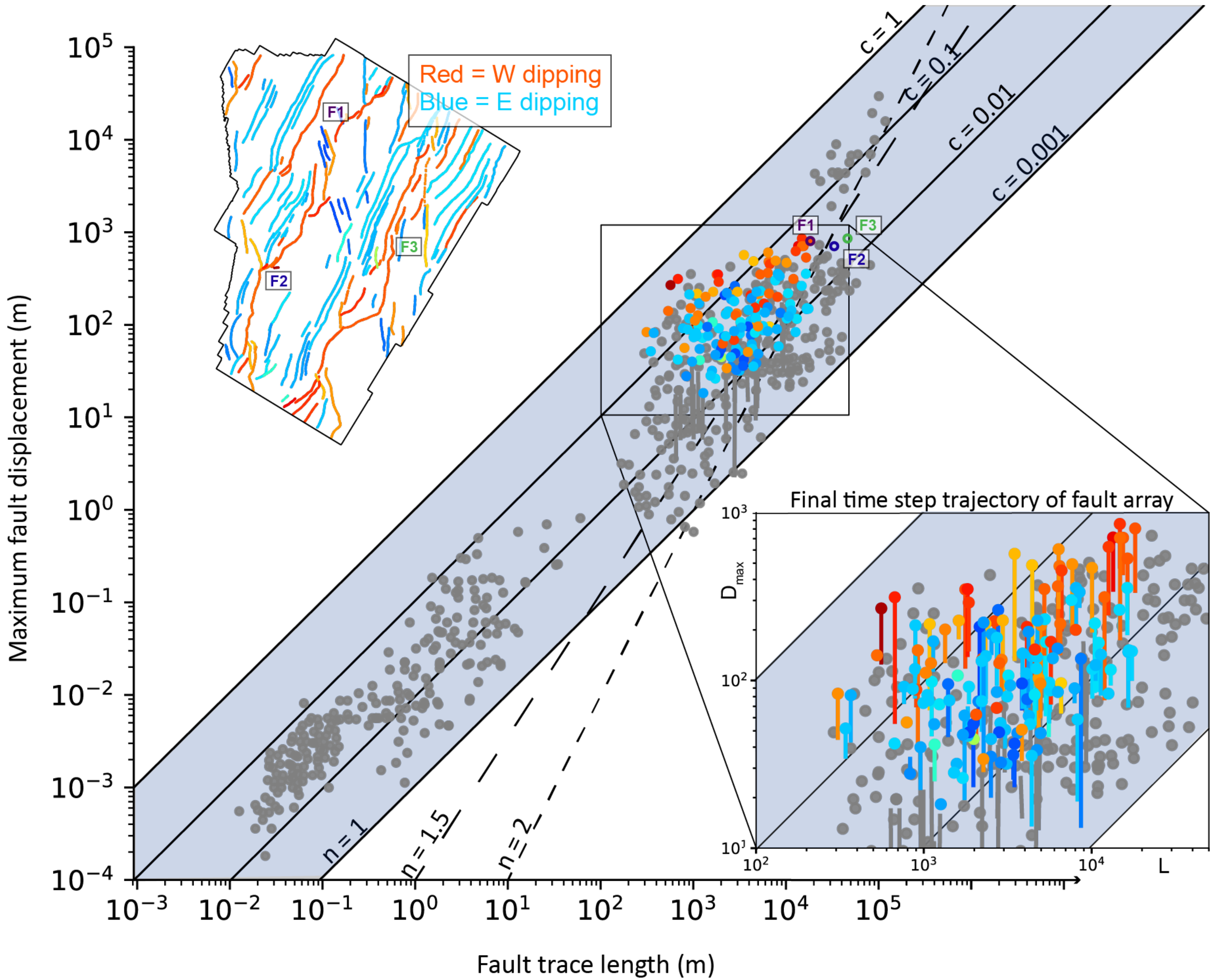

Figure 10. Our results plotted against global displacement-length data (in grey). Data is coloured by their dip (see Figure 7) whereby blue-coloured faults are east dipping, and red-coloured faults are west dipping. The inset shows the last 67% of rift history, as we connect our present-day values of fault geometry with their respective backstripped values.

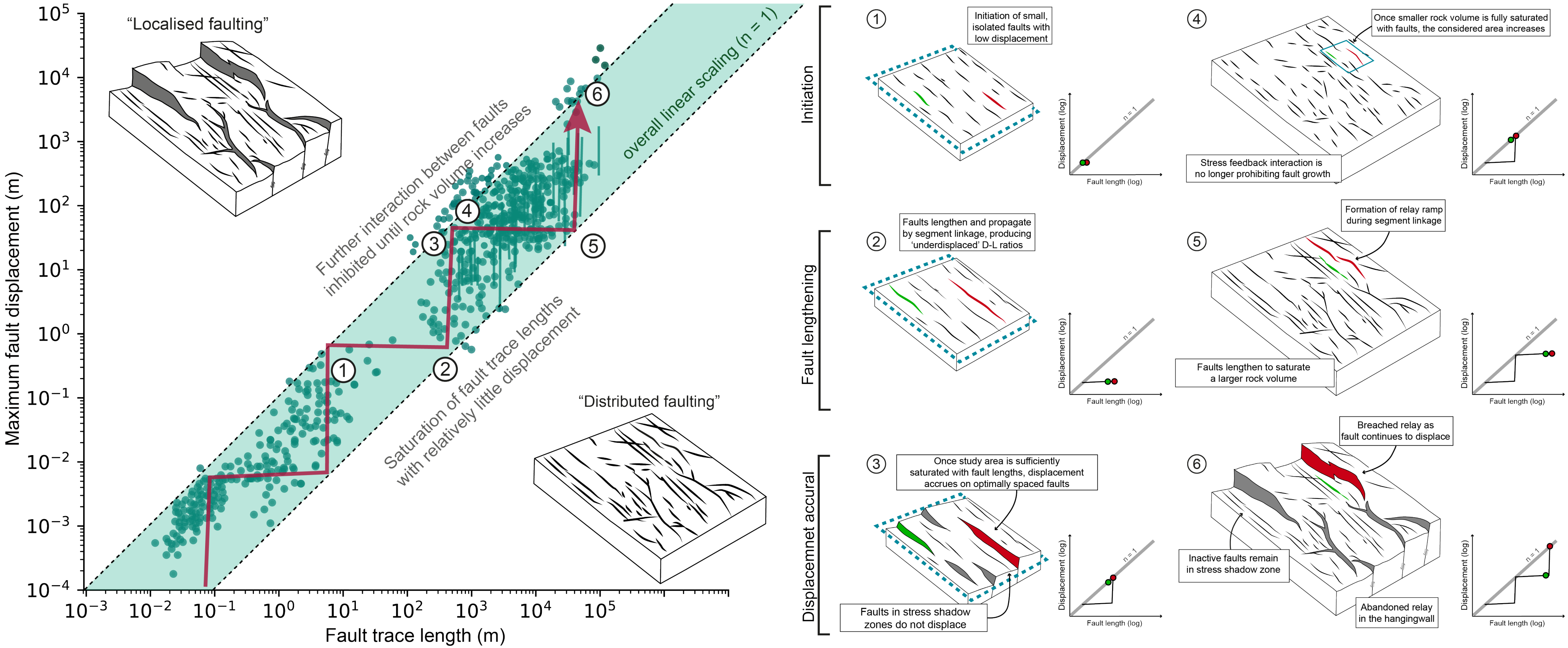

Figure 11. Our new proposed fault growth model, where the fault trajectory shows growth via alternating phases of fault lengthening (producing a near horizontal trajectory) and fault displacement (producing a near vertical trajectory). Stage 1, 2 and 3 are examples of initiation, linkage and localisation over a smaller region. Faults initiate as small numerous fault segments (1), then lengthen via segment linkage until the rock volume is sufficiently saturated, producing relatively under-displaced D-L values (2), displacement accrues on optimally located and spaced faults (3). Once the smaller region is saturated by fault lengths and displacement, the considered region increases, allowing the fault array to undergo initiation (4), lengthening (5) and localisation (6) again at a larger scale.